Combined coarse-grained molecular dynamics and finite-element study of light-activated deformation of photoresponsive polymers

Junghwan Moon,[1] Hayoung Chung [1],[2] and Maenghyo Cho[1],[3],[*]

[1]*Institute of Advanced Machines and Design, Seoul National University, Seoul, Republic of Korea*
[2]*School of Mechanical, Aerospace, and Nuclear Engineering, Ulsan National Institute of Science and Technology (UNIST),*
Ulsan, Republic of Korea
[3]*Division of Multiscale Mechanical Design, School of Mechanical and Aerospace Engineering,*
Seoul National University, Seoul, Republic of Korea

The azobenzene-containing crosslinked liquid crystalline polymer is a potential candidate for a stimuli-responsive soft robot, as it provides contactless actuation without the implementation of any separate component. For facilitating practical applications of this novel material, complicated and predefined motions have been realized by tailoring the chemical structure of the polymer network. However, conventional multiscale mechanical analysis, which utilizes the all-atom molecular dynamics to represent a microscopic model, is unsuitable for handling diverse material design parameters due to excessive computational costs. Hence, a multiscale optomechanical simulation framework, which combines the coarse-grained molecular dynamics (CG MD) and the finite-element (FE) method, is developed in this study. The CG MD simulation satisfactorily reproduces the light-induced phase transition and photosoftening effect on the mechanical properties. In particular, using the mesoscale analysis, the presented methodology can treat diverse morphology parameters (liquid crystal phase, spacer length, and crosslinking density) to observe the associated photodeformations. The photostrain and elastic modulus profiles in terms of photoisomerization ratio are implemented into the continuum-scale governing equation, which is based on the neoclassical elasticity theory. To efficiently reflect the light-induced large rotations of liquid crystal mesogens and the corresponding geometric nonlinearity, a corotational formulation is employed in the FE shell model. We examine the mesostructural-morphology-dependent photobending deformations of the nematic and smectic photoresponsive polymers (PRPs). In addition, the mesoscopic-texture-mediated unique 3D deformations are investigated by modeling the topological defects. This study offers insight into the engineering of PRP materials for designing the mechanical motions of smart actuators.

I. INTRODUCTION

Crosslinked liquid crystalline polymers (CLCPs), which possess photochromic azobenzene moieties, have drawn increasing attention owing to their reversible large deformations in response to actinic light irradiation. The conversion of the input photonic energy into mechanical action results from conformational changes in photosensitive liquid crystal (LC) mesogens and the elastomeric network [1]. Upon exposure to UV light, the rod-shaped *trans*-azobenzenes are photoisomerized into a kinked *cis*-configuration, which acts as an impurity for nematic alignment. The increased number of reacted molecules leads to a nematic-to-isotropic LC phase transition, accompanied by a contractive photostrain of the constituent polymer chains. These photoresponsive polymers (PRPs) are more suitable for small-scale robotic applications compared to conventional soft actuators, because they do not require on-board power and signal transmission components [2]. In fact, azobenzene-containing liquid crystalline polymers (LCPs) have been utilized as diverse photoresponsive actuators, such as biomimetic robots [3], motors [4], valves for fluid control [5], and shape-programmable elastic sheet [6,7].

Recent material science and engineering research has focused on realizing the targeting behavior of PRPs for more practical applications. To achieve this goal, elaborate designs of the LC state and polymer network structure have been developed. Above all, employment of more complex LC phases enables various photodeformation modes, besides simple bending of uniaxial nematic solids. Zhang *et al.* [8] demonstrated bidirectional actuation of smectic CLCPs, which retain both rotational and positional LC symmetries. Wie *et al.* [9] exploited the light-induced helical motion of twisted-nematic azopolymers for developing a photoresponsive rolling device. Furthermore, a preprogrammed 3D shape has been realized by imprinting complex LC director profiles through the surface alignment technique [7,10]. A pixelated array of these disclination-mediated topologies yields selective and localized controls of the photomechanical behavior [6,11]. An alternative to manipulating macroscopic photogenerated stress and strain is to modify the polymer architecture. Experimental studies have revealed that the spacer length of a PRP influences the alignment behavior of the azoderivatives and the corresponding photomechanical response [12,13].

*To whom correspondence should be addressed: mhcho@snu.ac.kr

Meanwhile, the increased crosslink density of the photosensitive molecules amplifies the actuating force [14].

To save the time and cost required to manufacture next-generation photoactuators, various computational studies have been conducted. From a microscopic viewpoint, Choi *et al.* [15] applied the photoreactive potential formalism to the all-atom molecular dynamics (AA MD) simulation to measure the molecular-scale photostrain of nematic solids. In contrast, a macroscopic response has been predicted using continuum-mechanics-based multiphysical analysis. Golubović and Lubensky [16] theoretically considered the unique spontaneous deformation of the LC gel under the isotropic-nematic transition. Jin *et al.* [17] derived order-mechanical coupling constitutive equations to describe the behavior of a liquid crystal elastomer (LCE) through an efficient construction of free energy. Lin *et al.* [18] conducted numerical finite-element (FE) simulations of light-triggered bending deformation by using a linearized stress-strain relationship of the PRP. Chung *et al.* [19] developed a 3D shell FE formulation to observe the thermo- and photoresponsive behaviors considering the geometric nonlinearity invoked by a large rotation of the nematic director. However, these exceptional continuum-scale studies could not explicitly reflect microstructure-dependent properties. To bridge the gap between the micro- and macroscopic scales, a multiscale optomechanical simulation scheme was devised [20]. In this study, the observables obtained using the AA MD simulations were directly upscaled to the photomechanics of the FE method. However, the exploitation of the conventional AA MD as a microscopic measurement tool imposes some limitations in the applicability. Because of the excessive computational demands for describing the pair interactions for each atom, only a simple nematic LCP structure with a fixed micromorphology can be reproduced. That is, the previously stated material design parameters cannot be properly handled. Accordingly, we developed a coarse-grained molecular dynamics (CG MD) model of the azopolymer network [21], which efficiently reduces the degrees of freedom (DOFs) and enables the construction of a larger macromolecular network. By using the proposed mesoscale model, a complex layered structure of the smectic CLCP, and its unique photomechanical response, were investigated.

Herein, extending the previous study, we present a multiscale CG-MD–FE model for a numerical investigation of light-actuated deformation. The CG MD simulation provides an explicit description of the sequential photoisomerization process and corresponding variations in the material properties. These mesoscale variables are implemented in the 3D FE analysis to explore the macroscale deformations. Notably, extension to the mesoscale simulation regime facilitates the establishment of a relationship between the mesostructural traits (LC phase, spacer length, and crosslinking density) and overall photomechanical performance. Furthermore, the proposed methodology is applied to realize not only simple bending deformations but also uncommon light-induced shapes assisted by the spatially varying mesostate. Another contribution of this work is that it accurately describes the evolution of the elastic modulus under the photochemical reaction. After the light irradiation, the *cis*-azobenzene molecules destruct the arrangement and the self-assembled structure of the PRP, which results in the photosoftening effect. Induced by the photoisomerization, a significant decrease of up to 2.5-fold has been observed in Young's modulus [22]. Although this mechanical degradation is not negligible, conventional continuum-scale studies on PRP materials have not considered it to derive the macroscopic deformation. Hence, in this study, the mechanical properties extracted from the stress-strain curves of the CG MD model are plugged into the FE formulation to address the photosoftening effect. We believe that our computational model will shed light on a deep understanding of the multiscale nature of the photoactivated deformation and a rational design of the advanced soft actuator.

II. SCALE-BRIDGING STRATEGY FOR OPTOMECHANICAL ANALYSIS

This section presents a bottom-up multiscale strategy to efficiently describe light-activated deformations. Figure 1 is a phenomenological illustration showing the origin of the photobending behavior. If the UV ray is irradiated to the PRP solid, the optical beam is absorbed and hence, the light intensity decays with depth. Accordingly, the number of photogenerated *cis* isomers, which is proportional to the local light intensity, also diminishes with the film's depth. From the atomistic or mesoscopic viewpoint, the photoisomerization from *trans*- to *cis*-state induces molecular shape change of azobenzenes, which deforms the entire polymer network and manipulates the mechanical properties. The mesoscale photostrain and inhomogeneous stiffness profiles in terms of *cis*-population are computed using the CG MD simulations. These mesoscale variables are upscaled to a continuous medium, and the light-induced bending moment and resulting macroscopic deformations are captured via the FE analysis. This section is organized as follows: Section II A presents the CG MD simulation scheme to reflect the underlying photoisomerization process. In Sec. II B, we prepare the multiscale parameters to describe the mesoscale response of the LCP network. Finally, the formalism and implementation of the optomechanical FE constitutive model are presented in Sec. II C.

A. CG MD simulation

In this study, a construction of the AA MD reference models is performed using the Forcite module of the Materials Studio package (BIOVIA, Inc.). The polymer consistent force field [23] is adopted to describe the interaction between the organic molecules. The van der Waals energy is calculated using the atom-based summation with a cutoff of 9.5 Å, and the Ewald summation is used to compute the Coulombic force. Mapping of the atomistic to CG model and derivation of the equivalent potentials are carried out via using the Mesocite module of the Materials Studio package (BIOVIA, Inc.). The Large-scale Atomic/Molecular Massively Parallel Simulator (LAMMPS) code, which was developed by the Sandia National Laboratory [24], is used to perform the long-time mesoscale photoisomerization simulation.

In general, systematic mapping from several atoms to virtual CG beads and derivation of the equivalent potential energy sets should be essentially carried out to reduce
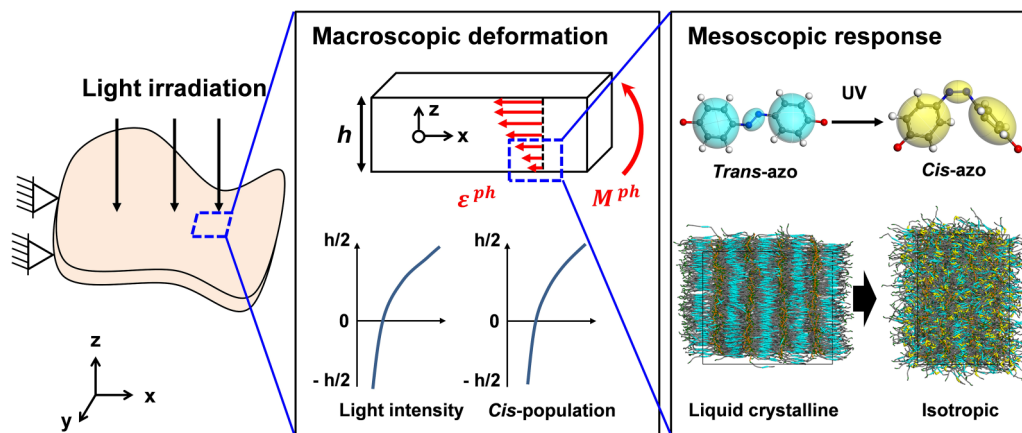
FIG. 1. Mesoscopic and macroscopic origins of the light-activated deformation behavior of the PRP.

the number of DOFs while preserving key aspects of the atomistic parent model. In order to examine the effect of elastomeric morphology on the photomechanical performance, the mesoscale polymer models with different spacer lengths and crosslink densities are constructed. The azobenzene-containing LCPs with 3 different numbers of the methylene units (6, 9, and 11) in the spacer group are prepared. Figure 2 shows the atomistic and coarse-grained configurations of the LC monomers and crosslinkers with different spacer lengths. The azobenzene unit is represented with a three-bead system, which consists of two P beads connected to a centered N bead. Acrylate spacer units are divided into C3, C2, and CO type beads. The C3 type bead corresponds to 3 methylene units or 2 methylene units and one oxygen atom which is connected with the azobenzene molecule. The C2 bead represents 2 methylene units or the vinyl group in the acrylates. The
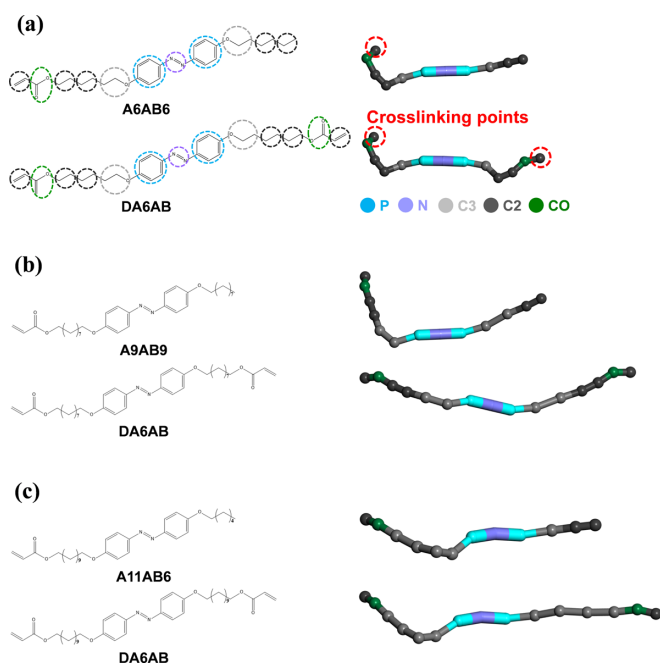

FIG. 2. Chemical structures and corresponding CG MD configurations of the LCPs with different spacer lengths: The numbers of the methylene groups in the spacer chain are (a) 6, (b) 9, and (c) 11.

remaining 2 oxygens and 1 carbon atom in the ester group are replaced with the CO bead. The CLCPs composed of the monomers shown in Fig. 2 have been successfully synthesized and utilized as photoresponsive actuators [4,8,25].

The crosslinking degree of the mesomolecules is modulated by changing the molar ratio between the acrylate LC monomers and the diacrylate crosslinking agents (9:1, 8:2, and 6:4). Before the curing simulation, a partially crosslinked polymer which consists of 20 LCPs is chosen as the unit molecule in order to prevent the requirement of excessive polymerization events. 96 unit molecules containing 1920 LC mesogens are inserted into an orthorhombic simulation box with the periodic boundary conditions. Initially, the azobenzene groups are oriented to the nematic direction (x axis). The CG bulk model is equilibrated by performing the conjugated gradient algorithm and *NPT* runs for 10 ns at 300 K and 0.1 MPa with a time step of 10.0 fs. The temperature and pressure are controlled via the Langevin thermostat [26] and the Berendsen barostat [27], respectively. Then, the polymerization of the complex LCP network is conducted by applying an *in situ* crosslinking scheme [28,29] to the prepared CG MD model. In this method, artificial bonds are generated whenever the distance between the reactive CG beads becomes shorter than a predefined cutoff during the dynamics simulation. The cutoff distance increases from 4.5 Å to 9.0 Å with an increment of 0.5 Å, and before shifting the cutoff, short *NPT* runs at 400 K for 3 ns are applied to construct the intermediate relaxed structure. At the first stage of the curing simulation, two reactive beads at both ends of the diacrylate crosslinks [see Fig. 2(a)] are primarily linked with surrounding monoacrylate monomers. This procedure imposes an elastomeric network structure on the CG model. The first step is completed when about 63% of the reactive beads of the crosslinking agents are reacted. Next, the remaining LC monomers are polymerized to form a long, stable, backbone structure until in total 40% of the reactive beads in the system have reacted. Finally, *NPT* runs at 400 K for 10 ns and at 300 K for 120 ns are applied to construct the ordered LC phase of the mesoscale model. The detailed polymerization scheme and structure of the crosslinked mesomolecule can be found in the previous study [21]. Table I lists the detailed information on the CLCP models considered in this study. For convenience, all PRP network models are simply named as "S*ab*X*cd*". The *ab* and *cd*

TABLE I. Basic information on the unit cells of the CG macromolecules with different spacer lengths and crosslinking densities.

System	Number of LC monomers	Number of LC crosslinkers	Average molecular weight (kg/mol)
S6X10	1728	192	8.25
S6X20	1536	384	10.67
S6X40	1152	768	19.63
S9X10	1728	192	9.76
S9X20	1536	384	13.06
S9X40	1152	768	19.72
S11X10	1728	192	9.63
S11X20	1536	384	12.15
S11X40	1152	768	24.70

stand for the number of methylene units in the spacer and the molar concentration of the crosslinking agent, respectively. As shown in Table I, the molecular weight of the mesomolecule increases with larger number of the crosslinking agents because the acrylate backbones are more densely connected.

To perform the mesoscale dynamics simulation, we derived new potential energy sets from the parent AA MD model. The CG potential energy can be divided into bonded energy (bond stretching and angle bending) and nonbonded energy terms. Meanwhile the intramolecular interaction energy is derived to describe the polymeric conformation of the CLCP network, and the intermolecular energy is elaborately optimized to reproduce both structural and thermodynamic properties. Figure 3 shows illustrative procedures to calculate the CG potential energies of each interaction type. Internal DOFs which contribute to the bonded interaction are bond length (l) between 2 adjacent beads and bond angle (θ) formed by 3 adjacent beads. Probability distributions of each conformational quantity [$P_{CG}(l)$ and $P_{CG}(\theta)$] are obtained from the reference AA MD trajectories of the LCP network model equilibrated at 400 K. The detailed procedures to construct the reference atomistic structures are given in the previous publication [21]. The CG bond length and angle potentials [$U_{CG}(l)$ and $U_{CG}(\theta)$] are obtained by Boltzmann inversion of the distributions:

$$U_{CG}(l) = -k_B T \ln[P_{CG}(l)/l^2], \qquad (1)$$

$$U_{CG}(\theta) = -k_B T \ln[P_{CG}(\theta)/\sin\theta]; \qquad (2)$$

k_B is the Boltzmann constant and T is the temperature of the reference state. Each structural distribution function is decomposed into a sum of Gaussian functions [30]. Hence, final functional forms of the CG bonded potentials are given as below:

$$U_{CG}(l) = -k_B T \ln\left[\sum_{i=1}^{n} a_i \exp\left\{-\left(\frac{l-l_i}{b_i}\right)^2\right\}\right], \qquad (3)$$

$$U_{CG}(\theta) = -k_B T \ln\left[\sum_{i=1}^{n} a_i \exp\left\{-\left(\frac{\theta-\theta_i}{b_i}\right)^2\right\}\right], \qquad (4)$$

where l_i and θ_i are the central peak positions of the ith Gaussian functions, and a_i and b_i are the fitted coefficients. The derived potential coefficients for the mesoscale PRP model are listed in Table II. Different potentials are applied to the distance between two C2 beads located at the spacer unit and the crosslinked backbone owing to the difference in geometry.

The radial distribution function (RDF) and density are the target properties to derive the CG noncovalent interaction energy. Unlike the bonded energy, simultaneous refinement of 15 different nonbonded interaction sets for 5 different bead types by using only one reference is very challenging. Accordingly, additional all-atom reference models are prepared. The crosslinked LCP structure is segmented into several small fragments to compute each potential separately. The isotropic fragment unit cells are composed of the 300 *trans*- (or *cis*-) azobenzenes, 200 octadecanes, and 400 octyl propanoates, respectively. The azobenzene unit cell is used to obtain P-P, P-N, and N-N interactions. The octadecanes are split into the C3 or C2 beads to derive the C3-C3 and C2-C2 interactions. Finally, the structural and thermodynamic properties of the octyl propanoate liquids are extracted to parametrize the CO-CO interaction. Next, a subsequent refinement process which consists of the iterative Boltzmann inversion (IBI) and pressure-correction (PC) methods is adopted to reproduce the multitarget properties. At first stage, the IBI method is applied to capture the RDF of the parent polymer. An initial guess of the nonbonded potential [$U_{CG,0}(r)$] can be obtained by taking a Boltzmann inverse of the target RDF [$g(r)$]:

$$U_{CG,0}(r) = -k_B T \ln[g(r)], \qquad (5)$$

where r is the separation between the CG beads. Applying the computed interaction energy at every iteration step, the *NVT* ensemble at 400 K for 8 ns is carried out to obtain the refined RDF. As shown in Fig. 3(c), the RDF of the 1st iteration is not the same with the target distribution. Therefore, the potential is gradually improved by adding a correction term, which can be expressed as

$$U_{CG,i+1}(r) = U_{CG,i}(r) - \beta k_B T \ln\left(\frac{g_i(r)}{g(r)}\right), \qquad (6)$$

where $g_i(r)$ is the RDF of the ith iteration and β is an adjustable constant. The repeated iterations are carried out until a target function (f_{target}), which measures the deviation from the target distribution, is below 1.0×10^{-4}. f_{target} can be calculated as the error integral:

$$f_{target} = \int_0^{r_c} \exp(-r)\{g_i(r) - g(r)\}^2 dr; \qquad (7)$$

r_c is the cutoff distance to compute the RDF, and it is set to 2 nm in this study. As f_{target} becomes lower than threshold, the mesoscale model has almost the same structural property as the parent model [Fig. 3(c)]. However, the pair interaction solely driven by the IBI cannot reproduce the exact density. Consequently, an attractive linear tail function is added to the previously derived energy in order to compute the pressure-corrected potential [$U_{CG}^{PC}(r)$] [31]:

$$U_{CG}^{PC}(r) = U_{CG}(r) - \gamma k_B T \left(1 - \frac{r}{r_c}\right). \qquad (8)$$
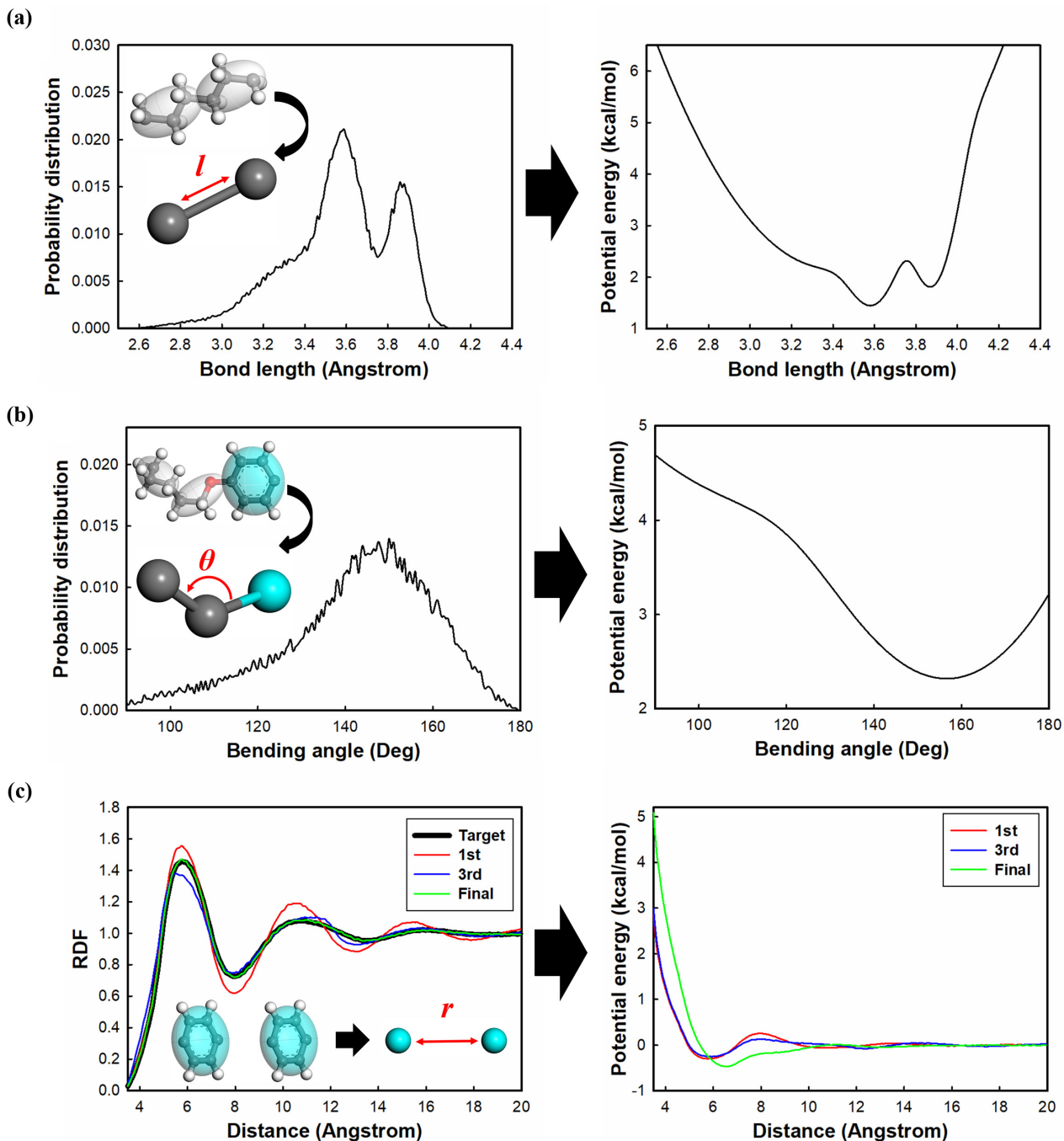
FIG. 3. Calculation of the CG potentials from the target properties of the AA MD system: (a) bond stretching, (b) bond angle bending, and (c) nonbonded interaction energies.

The adjustment of the potential via the PC method is carried out until the pressure of the CG model equals the target pressure (0.1 MPa). We utilized the IBI- and PC-based CG potentials to describe the mesogen-mesogen interactions (P-P, P-N, and N-N), which are the most significant factors to determine the LC phase, and the interactions between the same types of beads. Less important pair interactions between the different types are simplified by using the Lennard-Jones (LJ) 9-6 analytic function:

$$U_{CG}^{LJ}(r) = \varepsilon \left\{ 2\left(\frac{\sigma}{r}\right)^9 - 3\left(\frac{\sigma}{r}\right)^6 \right\}. \tag{9}$$

Table III lists the LJ parameters (ε: well depth and σ: the distance at which the potential reaches minimum value) of the interactions between the same CG beads. The pair interaction parameters for different types are calculated by the Lorentz-Berthelot mixing rules of $\varepsilon_{ij} = \sqrt{\varepsilon_i \varepsilon_j}$ and $\sigma_{ij} = (\sigma_i + \sigma_j)/2$. The elaborately determined CG interaction sets can predict the thermotropic phase transition behavior as well as the structural and thermodynamic characteristics of the LCP materials as shown in our previous work [21].

Finally, the photoisomerization reaction of the azobenzene groups is realized in the mesoscopic model. We focused on

TABLE II. Derived interaction parameters for the CG PRP model.

Parameters for bond-stretching interactions								
Type	a_1	b_1 (Å)	l_1 (Å)	a_2	b_2 (Å)	l_2 (Å)	a_3	b_3 (Å)	l_3 (Å)
P-N	0.691	0.077	3.216						
P-C3	0.286	0.082	3.797	0.095	0.164	3.698			
C3-C3	0.114	0.117	3.589	0.065	0.358	3.387	0.092	0.090	3.873
C3-C2	0.239	0.203	2.602	0.142	0.190	2.971			
C3-CO	0.211	0.088	3.281	0.171	0.218	3.002	0.027	0.168	2.539
C2-C2 (backbone)	0.441	0.110	2.609	0.334	0.125	2.379			
C2-C2 (terminal)	0.209	0.323	2.678	0.045	0.169	3.252			
C2-CO	0.937	0.104	2.416						

Parameters for angle-bending interactions								
Type	a_1	b_1 (deg)	θ_1 (deg)	a_2	b_2 (deg)	θ_2 (deg)	a_3	b_3 (deg)	θ_3 (deg)
P-N-P (*trans*)	1.332	9.071	179.9						
P-N-P (*cis*)	0.066	8.724	95.9						
P-C3-C3	0.005	32.990	115.7	0.053	21.790	157.0			
P-C3-C2	0.048	20.010	144.3						
N-P-C3	0.203	5.722	162.4	1.188	10.030	174.9			
C3-C3-C3	0.006	3.896	164.4	0.054	36.800	170.5	0.048	6.191	173.1
C3-C3-C2	0.040	27.824	154.5	0.108	13.692	178.7			
C3-C3-CO	0.032	35.100	153.5	0.090	11.620	179.0			
C3-C2-C2	0.010	21.580	109.3	0.009	14.050	136.1	0.050	21.130	165.5
C3-CO-C2	0.032	14.990	121.8	0.020	14.010	146.0			
C2-C2-C2	0.014	15.191	112.5	0.105	19.410	171.4			
C2-CO-C2	0.038	5.833	123.1	0.025	19.230	143.4	0.033	5.589	146.7
CO-C2-C2	0.025	5.129	76.27	0.013	4.172	95.7	0.014	24.850	98.4

Parameters for pair interactions		
Type	ε (kcal/mol)	σ (Å)
P-P	0.476	6.55
N-N	0.088	8.35
C3-C3	0.310	5.65
C2-C2	0.275	5.15
CO-CO	0.378	4.45

2 different structural variations induced by conversion from *trans*- to *cis*-molecules: (i) molecular shape change and (ii) corresponding variation in the intermolecular interaction between the mesogenic units. Figures 4(a) and 4(b) show how

TABLE III. Fitted coefficients to define a coupled relationship between phototriggered transition and shape change of the crosslinked polymer.

System		α	η
S6	X10	2.368	
	X20	2.430	
	X40	2.638	
S9	X10	2.679	0.903
	X20	2.803	0.706
	X40	3.010	0.561
S11	X10	2.801	1.132
	X20	2.932	0.852
	X40	3.138	0.513

to derive the CG photoswitching potentials in terms of the bonded and nonbonded interactions, respectively. The geometric change of the azobenzene itself is realized by switching the bending angle potential of the molecular axis (P-N-P). As shown in Fig. 4(a), the equilibrium angle changes from 180° to 96° under the light-induced configurational transition. The introduction of the isomerized molecules weakens the noncovalent interaction between the mesogens, which leads to a phase transition from LC to isotropic phase. To reproduce this disordering effect, the interaction energies between the *cis*-molecules [$U_{\mathrm{CG}}^{C-C}(r)$] and between the different isomers [$U_{\mathrm{CG}}^{T-C}(r)$] are additionally derived by using the 100% *cis*-azobenzene unit cell and mixture with 50% of the photoactivated molecules, respectively. Figure 4(b) shows gradual change in the CG energy between the aromatic rings (P-P) under the photochemical reaction. Rodlike trans-molecules in the unreacted PRP exhibit relatively stronger interaction, which retains the LC structure. Meanwhile, the well-depth energy decreases about 18% as the azobenzenes are converted into the *cis*-state, which breaks the molecular ordering. Likewise, the other mesogen-mesogen interactions (P-N and
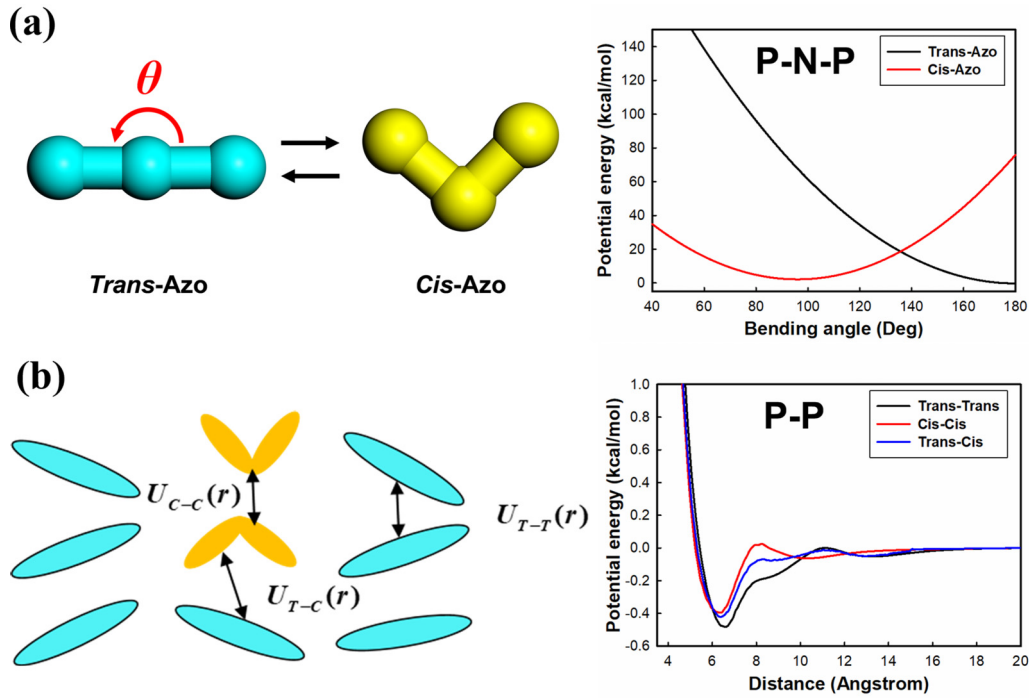
FIG. 4. Derivation of the CG photoswitching potentials to describe the changes in (a) molecular geometry and (b) the nonbonded interaction between the *trans-* and *cis*-isomers.

N-N) are switched to simulate the mesoscale phototriggered deformations.

B. Preparation of multiscale model parameters

As the UV-induced photoisomerization occurs, the PRP materials undergo a phase transition from LC to isotropic state. From the mechanical viewpoint, this mesophase behavior yields two significant effects: (i) deformation of the elastomeric network and (ii) degradation of the mechanical properties. Thus, it is necessary to capture the evolutions of the mesoscopic photostrain and mechanical modulus in response to the external light to predict the large-scale photodeformations. Especially, as shown in Fig. 1, because the absorbed photon energy and extent of the photochemical reaction decay with the penetration depth, the profile of the photomechanical properties should be parametrized in terms of the local population of the isomerized molecules (n_{cis}). Accordingly, the photoactivated mesomolecules with eight different photoisomerization ratios (n_{cis} = 0, 4, 8, 16, 20, 30, 50, and 70 percent) are modeled using the CG MD technique. The developed photoswitching interactions are applied to the designated fraction of the photoreactive sites to generate *cis*-azobenzenes. Then, the *NPT* run at 300 K is conducted for 150 ns to reproduce each deformed state.

The azobenzene-containing compounds considered in this study exhibit smectic-*A*–nematic (Sm-*A*–N) and nematic-isotropic (N-I) transitions under light irradiation. Because the macromolecular deformation mode is dependent on individual transition behaviors, the LC phase should be characterized by calculating the symmetry parameters. In the Sm-*A* phase, the mesogens are tightly assembled to form densely packed layers, which are periodically located along the nematic director.

The degree of this translational symmetry of the LC molecules is evaluated by calculating a 1D translational order parameter (τ):

$$\tau = \left\langle \left\| \exp\left(2\pi i \frac{\mathbf{r}_k \cdot \mathbf{n}}{d} \right) \right\| \right\rangle_k, \tag{10}$$

where $\mathbf{r}_k$ is the center of the mass position vector of the k th LC moieties, $\mathbf{n}$ is the nematic director, and d is the spacing between the adjacent smectic layers. As the photoisomerization proceeds, the layered structure is primarily broken, while the nematic alignment remains. The uniaxial ordering of the nematic molecules is quantified using the scalar orientational order parameter (s):

$$s = \left\langle \frac{3\cos^2\theta - 1}{2} \right\rangle, \tag{11}$$

where θ is the angle between the individual molecular axis of the LC molecules and long-range nematic director.

Deformation of the elastomeric network in response to the phase transition can be described as a change in the shape parameter (r) of the constituent polymer chains. The shape parameter, which specifies the shape anisotropy of the LCP molecule, can be simply calculated using the prepared mesomolecule models. In particular, this characteristic property acts as a link between the mesoscopic and macroscopic descriptions, because it is a key parameter for the continuum-scale governing equation of the equilibrium elastic response [32]. Here, r is expressed as a function of radius of gyration components of partially crosslinked polymer molecules:

$$r = \left\langle \frac{R_{\parallel}}{R_{\perp}} \right\rangle^2, \tag{12}$$

where $R_{\parallel}$ and $R_{\perp}$ are the radii of gyration components parallel and perpendicular to the director, respectively.

The light-induced collapse of the molecular alignment causes a large reduction in the elastic modulus, as well as deformations of the macromolecules. To evaluate this photo-softening effect, the mechanical behavior of the PRP network is analyzed using the CG MD model. Uniaxial tensile loading is applied along the oriented direction (x) under the *NPT* ensemble at 300 K. The nominal strain rate is $10^7/s$, and the applied strain gradually increases up to 0.15. The virial formula [33] is utilized to compute the stress at each deformed state, and the stress-strain curves of the CLCPs with different photoisomerization ratios (n_{cis}) are obtained. Mesoscale simulation data points are fitted to the analytic functional forms to extract the effective elastic moduli.

The stress-strain relationship of the nematic LCP is generally defined by the neoclassical theory, which combines the classical rubber elasticity and the molecular anisotropy induced by the LC order [16,32]. The neoclassical free energy density of nematic elastomers (F_N) can be expressed as

$$F_N = \frac{1}{2}\mu \mathrm{Tr}(l_0 \lambda^T l^{-1} \lambda), \tag{13}$$

where μ is the shear modulus of the crosslinked polymer network and λ is the deformation gradient tensor. Here, the subscript "0" denotes the quantities of the undeformed configuration. l_0 and l are the effective step length tensors, which record the polymeric shapes and directors of the initial and current states, respectively. They can be expressed as

$$l_0 = \mathbf{I} + (r_0 - 1)\mathbf{n}_0 \otimes \mathbf{n}_0, \quad l = \mathbf{I} + (r - 1)\mathbf{n} \otimes \mathbf{n}, \tag{14}$$

where $\mathbf{n}$ is the long-range director vector of the LC mesogens. The variable r can be calculated using Eq. (12). As the extension $\lambda_{xx} = \lambda$ is applied parallel to the nematic direction, the relaxations along the perpendicular directions should be $\lambda_{yy} = \lambda_{zz} = 1/\sqrt{\lambda}$ to minimize the elastic energy. Assuming a small imposed strain, the director and nematic order do not change crucially, which leads to $l_0 \simeq l$. Then, the free energy expressed in Eq. (13) can be simplified as

$$F_N = \frac{1}{2}\mu\left(\lambda^2 + \frac{2}{\lambda}\right). \tag{15}$$

The nominal stress is computed by differentiating F_N with respect to λ:

$$\sigma_N = \frac{\partial F_N}{\partial \lambda} = \frac{1}{2}\mu\left(\lambda - \frac{1}{\lambda}\right). \tag{16}$$

In the case of Sm-*A* elastomers, a geometric constraint term, which is relevant to rigidly embedded layers, is added to derive the smectic free energy (F_S):

$$F_S = \frac{1}{2}\mu\mathrm{Tr}(l_0\lambda^T l^{-1}\lambda) + \frac{1}{2}B\left(\frac{d}{d_0} - 1\right)^2, \tag{17}$$

where B is the layer modulus and d is the spacing between adjacent layers. The director of the deformed smectic solid and layer spacing change (d/d_0) can be computed assuming an affine deformation of the layers with the imposed strain [34]:

$$\mathbf{n} = \frac{\lambda^{-T} \cdot \mathbf{n}_0}{|\lambda^{-T} \cdot \mathbf{n}_0|}, \quad \frac{d}{d_0} = \frac{1}{|\lambda^{-T} \cdot \mathbf{n}_0|}. \tag{18}$$
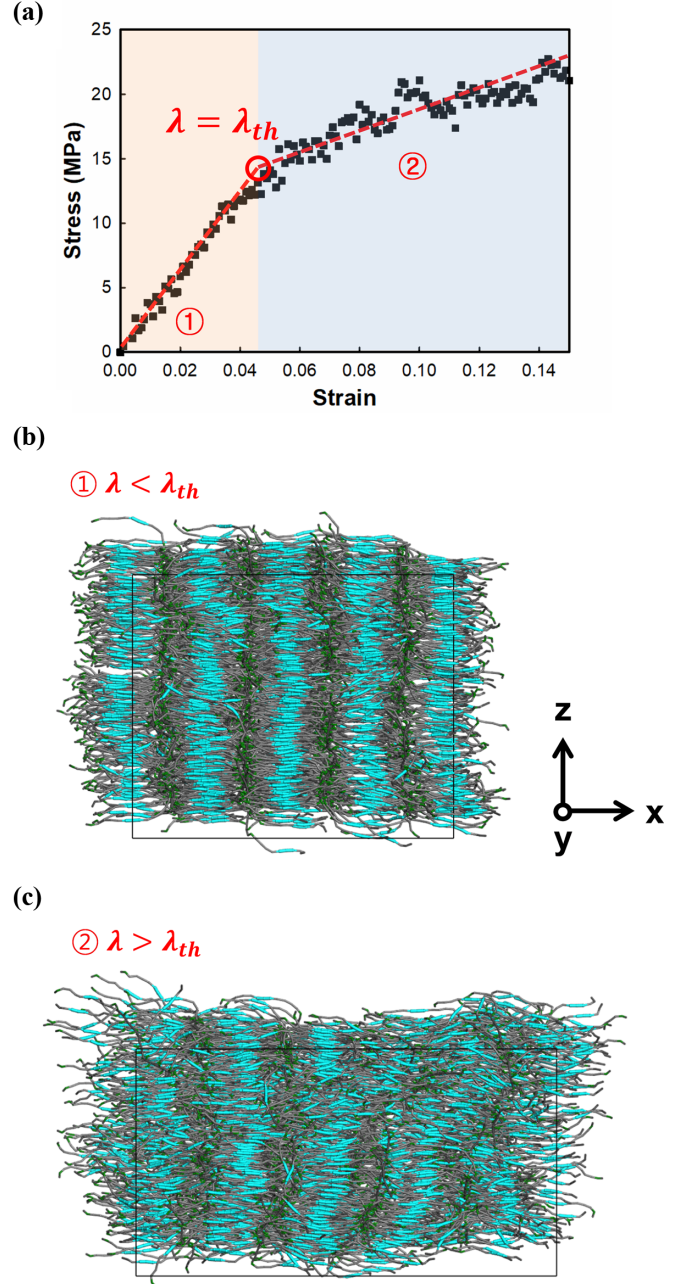

FIG. 5. (a) Stress-strain response and the configurations of the smectic azo-LCP models (b) before and (c) after the breakdown of the layers.

Unlike the nematic polymer, the Sm-*A* system exhibits an unusual nonlinear elastic response provoked by drastic microstructural variation. It has been revealed that as the uniaxial loading is applied parallel to the layer normal, the associated mechanical behavior can be divided into two regimes [35,36]. For small strains, the uniformly layered structure results in a relatively large elastic stiffness because the smectic layer modulus B is significantly larger than μ of the elastomeric network. However, if the applied deformation exceeds a threshold strain (λ_{th}), the mechanical modulus decreases remarkably. This unique mechanical behavior can be clearly observed using the CG MD simulation. Figure 5 shows the

generic stress-strain curve and structural characteristics of the Sm-*A* polymer in different deformed states. As shown in Fig. 5(a), the slope of the stress-strain curve decreases remarkably as the strain exceeds a specific value. In the small strain regime ($\lambda < \lambda_{\text{th}}$), the firmly assembled layers provide great mechanical resistance [Fig. 5(b)]. Meanwhile, as shown in Fig. 5(c), the smectic structure breaks down accompanied by the local rotation of the layer planes, which reduces the elastic stiffness at $\lambda > \lambda_{\text{th}}$.

The mechanical response of the smectic solids can be described using analytic functions considering the layer rotation at a singular edge. As the extension $\lambda_{xx} = \lambda$ along the layer normal direction is applied, the associated deformation tensor is expressed as follows:

$$\boldsymbol{\lambda} = \begin{bmatrix} \lambda & 0 & 0 \\ 0 & \lambda_{yy} & 0 \\ \lambda_{zx} & 0 & \lambda_{zz} \end{bmatrix}. \tag{19}$$

The shear λ_{zx} starts to occur as the elongation reaches the critical strain, and induces rotation of the layers. Then, the elastic free energy can be rearranged by inserting Eqs. (14), (18), and (19) into Eq. (17):

$$F_S = \frac{1}{2}\mu\left[\lambda_{zz}^2 + \frac{1}{\lambda_{zz}^2\lambda^2} + \lambda_{zx}^2 + \frac{(\lambda_{zz}^2 + r\lambda_{zx}^2)\lambda^2}{\lambda_{zz}^2 + \lambda_{zx}^2}\right]$$
$$+ \frac{1}{2}B\left(\frac{\lambda\lambda_{zz}}{\sqrt{\lambda_{zz}^2 + \lambda_{zx}^2}} - 1\right)^2. \tag{20}$$

The transverse contraction λ_{yy} is eliminated using the incompressibility condition [$\det(\boldsymbol{\lambda}) = 1$]. Before the smectic layer starts to rotate, the shear deformation does not appear ($\lambda_{zx} = 0$). However, after the mechanical instability point, λ_{zx} is generated with singular rotation. λ_{zz} and λ_{zx} can be obtained as functions of λ and λ_{th} by minimizing the energy with some simplifications [34]:

$$\lambda_{zz} = \frac{\sqrt{\lambda_{\text{th}}}}{\lambda}, \quad \lambda_{zx} = \pm\sqrt{\frac{1}{\lambda_{\text{th}}} - \frac{\lambda_{\text{th}}}{\lambda^2}}. \tag{21}$$

Finally, the analytic solutions of elastic energy and corresponding stress-strain relationship, which are split into two parts with respect to the deformation regime, are given as Eqs. (22) and (23), respectively:

$$F_S = \begin{cases} \frac{1}{2}\mu\left(\lambda^2 + \frac{2}{\lambda}\right) + \frac{1}{2}B(\lambda - 1)^2, & (\lambda < \lambda_{\text{th}}), \\ \frac{1}{2}\mu\left[\lambda_{\text{th}}^2 + \frac{2}{\lambda_{\text{th}}} + r(\lambda^2 - \lambda_{\text{th}}^2)\right] + \frac{1}{2}B(\lambda_{\text{th}} - 1)^2, \\ \quad (\lambda > \lambda_{\text{th}}), \end{cases} \tag{22}$$

$$\sigma_S = \begin{cases} \mu\left(\lambda - \frac{1}{\lambda^2}\right) + B(\lambda - 1), & (\lambda < \lambda_{\text{th}}), \\ \mu r\lambda, & (\lambda > \lambda_{\text{th}}). \end{cases} \tag{23}$$

The stress-strain curves of the CG unit cells with different n_{cis} values are fitted to Eq. (16) to extract the shear modulus (μ) of the nematic solids. For the Sm-*A* polymer, two unknown variables (μ and B) are simply calculated by fitting the data points in two different deformation regimes to Eq. (23).

C. Nonlinear FE implementation

The macroscopic behavior of the PRP is derived by adopting the continuum-scale quasisoft elasticity model [18], which reflects a strong coupling between the mechanical deformation and the nematic order of the LCs. Starting from neoclassical elasticity, Eq. (13) for nematic free energy can be rearranged as

$$F_N = \frac{1}{2}\mu\text{Tr}(\mathbf{g}^{-1}\boldsymbol{\lambda}\mathbf{g}_0\boldsymbol{\lambda}^T) = \frac{1}{2}\mu\text{Tr}(\mathbf{g}^{-1}\mathbf{C}), \quad \mathbf{C} = \boldsymbol{\lambda}\mathbf{g}_0\boldsymbol{\lambda}^T, \tag{24}$$

where $\mathbf{C}$ is the effective Cauchy-Green tensor, and $\mathbf{g}_0$ and $\mathbf{g}$ are the metric tensors of the initial and current states, respectively. They are calculated by making the step length tensor have a unit determinant:

$$\mathbf{g}_0 = \boldsymbol{l}_0/\det(\boldsymbol{l}_0)^{1/3}, \quad \mathbf{g} = \boldsymbol{l}/\det(\boldsymbol{l})^{1/3}. \tag{25}$$

It was found that the current polymeric conformation tensor ($\mathbf{g}$) becomes coaxial with $\mathbf{C}$ because the nematic director is adjusted by the applied deformations [17]. Accordingly, the eigenvectors of the $\mathbf{C}$ matrix coincide with those of $\mathbf{g}$. Considering this coaxiality, the Cauchy stress of the incompressible nematic polymers has the following expression:

$$\boldsymbol{\sigma}_N = -p\mathbf{I} + \mu\mathbf{g}^{-1}\mathbf{C} = -p\mathbf{I} + \mu\sum_{i=1}^{3} g_i^{-1}C_i\mathbf{e}_i \otimes \mathbf{e}_i. \tag{26}$$

Here, p is the hydrostatic pressure, $\mathbf{e}_i$ indicates the eigenvectors, and g_i and C_i are the corresponding eigenvalues. Uniaxial metric tensors can be expressed in terms of the polymeric shape parameter by inserting Eq. (14) into Eq. (25):

$$\mathbf{g}_0 = r_0^{-1/3}\mathbf{I} + (r_0^{2/3} - r_0^{-1/3})\mathbf{n}_0 \otimes \mathbf{n}_0,$$
$$\mathbf{g} = r^{-1/3}\mathbf{I} + (r^{2/3} - r^{-1/3})\mathbf{n} \otimes \mathbf{n}. \tag{27}$$

The final expression for the stress-stretch relation is derived by inserting Eq. (27) into Eq. (26):

$$\boldsymbol{\sigma}_N = -p\mathbf{I} + \mu r^{1/3}\left[\mathbf{C} - \left(1 - \frac{1}{r}\right)C_m\mathbf{n} \otimes \mathbf{n}\right], \tag{28}$$

where the current director $\mathbf{n}$ coincides with the eigenvector of $\mathbf{C}$ with the largest eigenvalue C_m (i.e., $\mathbf{Cn} = C_m\mathbf{n}$).

A direct implementation of the above nonlinear constitutive relation [Eq. (28)] into the classical FE formulation is very complicated. It is because of the soft elasticity of the LCEs under large stretching behavior: the long-range director of the mesogens rotates without energy cost. This unusual behavior brings about nonconvex free energy and generation of the singular stiffness matrix due to the vanishing of certain shear modulus. Thus, the modified semisoft elastic energy and additional solving technique have been utilized to implicitly treat the complex nonconvexity [17,37]. However, in this study, the constitutive model is linearized to simplify the photomechanical behavior of the PRP and to work directly on the stress-strain relation obtained after the minimization of the free energy. It is reasonable because the practical bending of the PRP is induced not by the large in-plane stretching but by the inhomogeneous in-plane contraction along the thickness. Other previous studies have adopted the linearized quasisoft governing equation of the neatmic LCEs and satisfactorily reproduced the light-induced bending behavior using

the FE formulations [18,19]. The linearization approach starts from introducing the displacement gradient $\mathbf{H} = \lambda - \mathbf{I}$ to the Cauchy-Green tensor:

$$\mathbf{C} = (\mathbf{H} + \mathbf{I})\mathbf{g}_0(\mathbf{H} + \mathbf{I})^T = \mathbf{g}_0 + \mathbf{Hg}_0 + \mathbf{g}_0\mathbf{H}^T = \mathbf{g}_0 + 2\boldsymbol{\varepsilon}_g. \tag{29}$$

The high-order term $\mathbf{Hg}_0\mathbf{H}^T$ is neglected, and the effective infinitesimal strain $\boldsymbol{\varepsilon}_g = (\mathbf{Hg}_0 + \mathbf{g}_0\mathbf{H}^T)/2$ contains symmetric Cauchy strain ($\boldsymbol{\varepsilon}$) and skew-symmetric rotation ($\boldsymbol{\omega}$) parts:

$$\boldsymbol{\varepsilon}_g = \tfrac{1}{2}(\boldsymbol{\varepsilon}\mathbf{g}_0 + \mathbf{g}_0\boldsymbol{\varepsilon}) + \tfrac{1}{2}(\boldsymbol{\omega}\mathbf{g}_0 - \mathbf{g}_0\boldsymbol{\omega}). \tag{30}$$

The current nematic director is defined as an initial director plus deformation-induced rotation ($\delta\mathbf{n}$):

$$\mathbf{n} = \mathbf{n}_0 + \delta\mathbf{n}. \tag{31}$$

By substituting Eqs. (29) and (31) into $\mathbf{Cn} = C_m\mathbf{n}$ and neglecting the high-order term, we can obtain

$$C_m = r_0^{2/3} + 2\mathbf{n}_0 \cdot \varepsilon_g \cdot \mathbf{n}_0, \tag{32}$$

$$\delta\mathbf{n} = \frac{2r_0^{1/3}}{r_0 - 1}[\varepsilon_g \cdot \mathbf{n}_0 - (\mathbf{n}_0 \cdot \varepsilon_g \cdot \mathbf{n}_0)\mathbf{n}_0]. \tag{33}$$

The linearized stress-strain relation can be obtained by inserting Eqs. (29)–(33) into Eq. (28):

$$\boldsymbol{\sigma}_N = -p\mathbf{I} + 2\mu\left(\frac{r}{r_0}\right)^{1/3}\left\{\begin{array}{l} \boldsymbol{\varepsilon} - \left[1 - \frac{r_0+1}{2(r_0-1)}\frac{r_0-r}{r}\right][\mathbf{n}_0(\boldsymbol{\varepsilon} \cdot \mathbf{n}_0) + (\boldsymbol{\varepsilon} \cdot \mathbf{n}_0)\mathbf{n}_0] \\ + \frac{2r_0}{r}\frac{r-1}{r_0-1}(\mathbf{n}_0 \cdot \boldsymbol{\varepsilon} \cdot \mathbf{n}_0)\mathbf{n}_0\mathbf{n}_0 + \frac{r_0-r}{2r}[\mathbf{n}_0\mathbf{n}_0 + \mathbf{n}_0(\boldsymbol{\omega} \cdot \mathbf{n}_0) + (\boldsymbol{\omega} \cdot \mathbf{n}_0)\mathbf{n}_0] \end{array}\right\}. \tag{34}$$

Note that the stress induces rotation of mesogenic alignment as well as an infinitesimal strain, which reflects the light-induced microstructural variation of the LCP network. Because the thickness of the practically used PRP strip is sufficiently small compared to its length [4,38], the plane stress condition is applied. Additional constraints are that (i) both initial and current nematic directors are located in-plane ($n_3^0 = n_3 = 0$) and (ii) the volume is conserved after light-induced deformation [tr($\boldsymbol{\varepsilon}$) = 0]. Under these conditions, the tensorial form of the mechanical equilibrium (the Greek indices are 1 or 2) is prepared as follows:

$$\begin{aligned}\sigma_{\alpha\beta}^N &= 2\mu\left(\frac{r}{r_0}\right)^{\frac{1}{3}}\left[\begin{array}{l} -\delta_{\alpha\beta}(\varepsilon_{11} + \varepsilon_{22}) + \varepsilon_{\alpha\beta} - \left\{1 - \frac{r_0+1}{2(r_0-1)}\frac{r_0-r}{r}\right\}\left\{\varepsilon_{\beta\gamma}n_\alpha^0 n_\gamma^0 + \varepsilon_{\alpha\gamma}n_\beta^0 n_\gamma^0\right\} \\ + \frac{2r_0}{r}\frac{r-1}{r_0-1}\left(\varepsilon_{\eta\psi}n_\eta^0 n_\psi^0\right)n_\alpha^0 n_\beta^0 + \frac{r_0-r}{2r}\left\{n_\alpha^0 n_\beta^0 + \omega_{\beta\gamma}n_\alpha^0 n_\gamma^0 + \omega_{\alpha\gamma}n_\beta^0 n_\gamma^0\right\} \end{array}\right] \\ &= \sigma_{\alpha\beta}^0\left(\varepsilon_{\alpha\beta}, \omega_{\alpha\gamma}, n_\alpha^0, r, r_0\right) + \sigma_{\alpha\beta}^{\mathrm{ph}}\left(n_\alpha^0, r, r_0\right). \end{aligned} \tag{35}$$

As shown in Eq. (35), the internal elastic stress ($\sigma_{\alpha\beta}^0$) and photostress ($\sigma_{\alpha\beta}^{\mathrm{ph}}$) are dependent on the light-induced property changes. Similarly, the mechanical-order coupling relation of the Sm-*A* polymer can be developed by considering the layer dilation energy, layer spacing change, and affine deformation of the layer normal [Eqs. (17) and (18)]:

$$\sigma_{\alpha\beta}^S = \mu\left(\frac{r}{r_0}\right)^{1/3}\left[\begin{array}{l} 2\delta_{\alpha\beta}(\varepsilon_{11} + \varepsilon_{22}) + 2\varepsilon_{\alpha\beta} + \{2r_0 - \frac{r_0}{r} - 1\}\left\{\varepsilon_{\beta\gamma}n_\alpha^0 n_\gamma^0 + \varepsilon_{\alpha\gamma}n_\beta^0 n_\gamma^0\right\} \\ + \left\{4\left(\frac{r_0}{r} - r_0\right) + \frac{B}{\mu}\left(\frac{r}{r_0}\right)^{-1/3}\right\}\left(\varepsilon_{\eta\psi}n_\eta^0 n_\psi^0\right)n_\alpha^0 n_\beta^0 \\ + \frac{r_0-r}{r}\left\{n_\alpha^0 n_\beta^0 + \omega_{\beta\gamma}n_\alpha^0 n_\gamma^0 + \omega_{\alpha\gamma}n_\beta^0 n_\gamma^0\right\} \end{array}\right]. \tag{36}$$

A detailed derivation procedure can be found in a previous numerical study [39].

Despite the use of the linearized governing equation, the light-induced conversion of the 2D thin strip into 3D complex shapes in reality requires a description of the large displacement of the structure. Accordingly, the element-independent corotational (EICR) formulation [40] is adopted to account for the geometric nonlinearity. The EICR formulation separates the rigid-body motion and deformation purely based on the kinematics, which is a distinguished feature compared to other solving techniques. Because the extraction of pure deformation is conducted independently of the element-wise calculations, this method enables the extension of the linear element to be used in the geometric nonlinear context. Figure 6 shows three independent configurations required for describing the EICR kinematics: (i) undeformed (Ω^0), (ii) deformed (Ω^D), and (iii) corotated (Ω^R) configurations. The corotated frame is a theoretical concept of the intermediate state between the initial and deformed frames, and can be obtained through rigid-body translation and rotation of the undeformed body. The element-wise pure deformation ($\bar{\mathbf{u}}_d$) and

rotation ($\bar{\boldsymbol{\theta}}_d$) can be filtered out from the global displacement by comparing the corotated system with the finally deformed state. The overbar and subscript d indicate the properties related to the local coordinate and pure deforming portions, respectively. Equation (37) describes the filtration process of EICR formulation:

$$\delta\bar{\mathbf{d}}_d = \begin{Bmatrix} \delta\bar{\mathbf{u}}_d \\ \delta\bar{\boldsymbol{\theta}}_d \end{Bmatrix} = \bar{\mathbf{H}}\bar{\mathbf{P}}\mathbf{T}\begin{Bmatrix} \delta\mathbf{u} \\ \delta\phi \end{Bmatrix} = \boldsymbol{\Lambda}\begin{Bmatrix} \delta\mathbf{u} \\ \delta\phi \end{Bmatrix}. \tag{37}$$

First, the matrix $\mathbf{T}$ is employed to transform the global nodal displacement ($\delta\mathbf{u}$) and spin ($\delta\phi$) into the quantities of the local corotational coordinate. Then, the projection matrix $\bar{\mathbf{P}}$ is utilized to filter out the rigid-body motions. Finally, the element-wise pure deformation ($\delta\bar{\mathbf{d}}_d$) can be computed using $\bar{\mathbf{H}}$, which eliminates the gap between two pseudovectors $\boldsymbol{\theta}$ and ϕ. A conventional Newton-Raphson algorithm with an adaptive step-size technique [41] is used to obtain a nonlinear solution. At this stage, the locally consistent tangential stiffness matrix and the residual force can be computed using
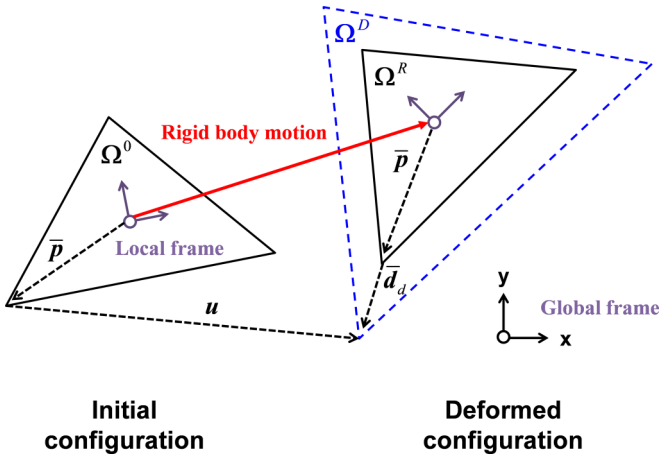
FIG. 6. Illustrative description of the kinematics-based filtration of the EICR formulation.

the first-order derivatives of the auxiliary matrices in Eq. (37) [19].

A triangular three-node linear shell element is employed to perform the FE analysis. Each node has six DOFs [nodal displacements (u_1, u_2, u_3) and rotations (θ_1, θ_2, θ_3)]. The intrinsic material properties of the LCP network (initial director, shape parameter, and elastic moduli) are individually defined at each element. Based on the variational principle, a set of equilibrium equations is obtained from the linear shell element formulation as follows:

$$
\begin{aligned}
\delta W &= \int_\Omega \delta(\boldsymbol{\varepsilon}^0 - z\hat{\mathbf{k}})(\boldsymbol{\sigma}^0 - \boldsymbol{\sigma}^{\text{ph}})dV \\
&= \delta\bar{\mathbf{d}}_d \cdot \bar{\mathbf{K}}^e \cdot \bar{\mathbf{d}}_d - \delta\mathbf{d}_d \cdot \bar{\boldsymbol{\Sigma}}^{\text{ph}},
\end{aligned}
\tag{38}
$$

where $\bar{\boldsymbol{\Sigma}}^{\text{ph}}$ comprises light-induced stress and moment resultants ($\hat{\mathbf{N}}^{\text{ph}}$ and $\hat{\mathbf{M}}^{\text{ph}}$), and the consistent stiffness matrix $\bar{\mathbf{K}}^e$ is calculated as a sum of matrices for each contribution:

$$
\bar{\boldsymbol{\Sigma}}^{\text{ph}} = \{\hat{\mathbf{N}}^{\text{ph}}, \hat{\mathbf{M}}^{\text{ph}}\}^T, \quad \bar{\mathbf{K}}^e = [\bar{\mathbf{K}}^m + \bar{\mathbf{K}}^b + 2\bar{\mathbf{K}}^{mb}],
$$

$$
\bar{\mathbf{K}}^m = \int \mathbf{B}^{\varepsilon T}\hat{\mathbf{A}}\mathbf{B}^\varepsilon dA, \quad \bar{\mathbf{K}}^b = \int \mathbf{B}^{\kappa T}\hat{\mathbf{D}}\mathbf{B}^\kappa dA,
$$

$$
\bar{\mathbf{K}}^{mb} = \int \mathbf{B}^{\varepsilon T}\hat{\mathbf{B}}\mathbf{B}^\kappa dA.
\tag{39}
$$

The superscripts m, b, and mb denote the stiffness matrices for membrane, bending, and coupled behaviors of the shell element, respectively. $\mathbf{B}$ is the strain matrix, where ε and κ denote the strain-displacement and strain-curvature relations, respectively. The optimal triangular [42] and the discrete Kirchhoff triangular [43] shell elements are exploited to handle the membrane and bending behaviors, respectively. Because the FE simulation must reflect the nonuniform local deformation and modulus profiles, the stiffness and photoresultant matrices are computed using a numerical integration with 250 thickness integration points, which is based on Simpson's rule.

The spatial profiles of the light intensity and the corresponding conversion ratio of the photoactive molecules are obtained to perform the multiphysical analysis. First, the decaying effective light intensity (I_{eff}) along the material

thickness is modeled using the Lambert-W function (W_L) [44]:

$$
I_{\text{eff}} = W_L\big[\exp\big(I_{\text{eff}}^0 - z/d\big)\big],
\tag{40}
$$

where I_{eff}^0 is the maximal intensity of the incident light at the surface, z is the penetration coordinate, and d is the characteristic saturation depth of light. The effective light intensity can be alternatively defined as $I_{\text{eff}} = \tau_{cis}\Gamma I$, where I is the light intensity, Γ is the absorption ratio, and τ_{cis}^{-1} is the *cis*-state lifetime. Then, a temporal evolution of the photoisomerization ratio (n_{cis}) profile is obtained by solving the photodynamics differential equation. Considering both UV-induced *trans*-to-*cis* conversion and thermal back-reaction, the steady-state *cis*-population (n_{cis}^∞) can be given as follows [44]:

$$
n_{cis}^\infty = \frac{\tau_{cis}\Gamma I}{1 + \tau_{cis}\Gamma I} = \frac{I_{\text{eff}}}{1 + I_{\text{eff}}}.
\tag{41}
$$

As shown in Fig. 1 and Eq. (41), the presented multi-scale simulation defines the local n_{cis} profile in terms of the input light intensity. Moreover, the mesoscale intrinsic properties in terms of the external light condition are extracted using the CG MD simulation. The phase-dependent conformational variation in response to the light stimuli is captured using the shape parameter [$r(n_{cis})$]. Moreover, the elastic moduli [$\mu(n_{cis})$ and $B(n_{cis})$] vary with respect to the out-of-plane position of the PRP strip, analogously to the functionally graded material, to explicitly express the photosoftening effect. These profiles are imported into the FE equilibrium equation [Eqs. (35) and (36)] to compute the consistent stiffness matrix, external photostress, and corresponding macroscopic photodeformation fields.

III. RESULTS AND DISCUSSION

A. Morphology-dependent photomechanical properties

Figure 7 shows the influence of spacer length on the initial LC structure of the PRP network. As shown in Fig. 7(a), the mesogens of the S6X40 system only possess the rotational symmetry ($s = 0.51$), which implies the development of a uniaxial nematic phase. Meanwhile, the equilibrated S9X40 has both orientational and translational orders ($s = 0.64$ and $\tau = 0.18$), and the LCs are more aligned compared to the S6 polymer [Fig. 7(b)]. The LCP which has the longest constituent polymer chains shows a deep Sm-A phase, as seen in Fig. 7(c), with the largest order parameters ($s = 0.86$ and $\tau = 0.64$). That is, a longer sparer length helps the whole system to exhibit a more complicated LC structure and an improved arrangement. The observed phenomenon agrees well with the result of the experimental studies [4,8,25]. As the length of the flexible polymer chain increases, the constraint on the orientational and translational symmetries of the azobenzene molecules is weakened. Furthermore, a more uncoiled polymeric conformation of the methylene units contributes to the arrangement of rigid mesogen groups.

Next, the morphology-dependent mesophase behavior is investigated. Figure 8(a) shows the sequential Sm-A–N–I phase transition induced by gradually increasing the number of isomerized groups. In the case of spacer 11 polymers, the self-assembled smectic layer is primarily broken with a low n_{cis} value of about 20%–30%. At this stage, the azobenzenes are still aligned to the long-range direction, which means that

(a)

z

y — x

Spacer 6

(b)
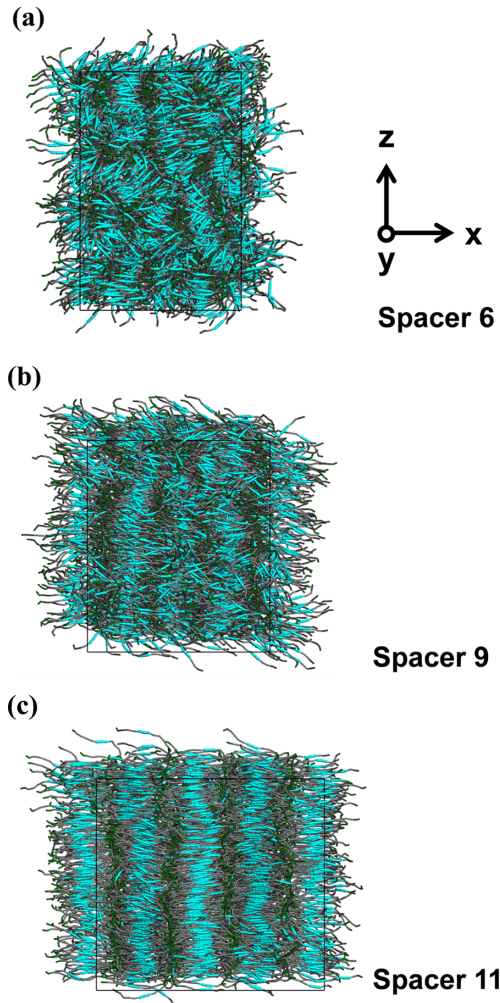
Spacer 9

(c)

Spacer 11

FIG. 7. Mesoscale configurations of the PRP networks which hold the different spacer lengths: (a) S6X40, (b) S9X40, and (c) S11X40 polymers.

the CLCP network is transformed into a nematic structure. Then, with increasing the n_{cis} up to 50%–70%, the system becomes the isotropic state without any symmetric order. Figures 8(b), 8(c), and 8(d) show the photon-assisted variations of the LC order parameters. These evolutions of the structural parameters reveal that the crosslinking density as well as the spacer length of the LCP affects the phase behavior. Regardless of the spacer length, s and τ increase with the increment of the concentration of the diacrylate crosslinking agents. This trend is consistent with that of the experimentally measured birefringence and polarized absorption spectra [45]. The crosslinking points between the polymeric backbones tightly fix the anisotropic shape and alignment of the network. The initial polymeric architecture also decides the phase transition pathway. Meanwhile the spacer 6 LCPs exhibit only N-I transition; the polymers with longer spacers show the light-activated transition among three different phases (Sm-A–N–I). As shown in Figs. 8(c) and 8(d), the translational order parameter of the S9 system decreases to less than 0.1 at $n_{cis} = $ 15%–20%, whereas more *cis*-molecules ($n_{cis} = $ 30%–50%) are required to break the layered structure of S11 polymers. These results indicate that the phase transition points under

the same light condition can be controlled by manipulating the length of the polymer chain. Another notable point is that, as the crosslinking density increases, the PRP sustains higher-order parameters during and even after the photochemical reaction process.

Variations in the mesophase behavior with respect to the microscopic morphology parameters influence the temporal evolution of the macromolecular deformation. Figure 9 shows the shape parameters of diverse azopolymers as a function of n_{cis}. As seen in Fig. 9(a), the shape anisotropy of the nematic S6 polymer decreases under the photoresponsive N-I transition. On the other hand, the sequential transformation of Sm-A polymers, especially for the S11 system, causes a shift in the deformation modes. During the Sm-A–N transition within a low *cis*-population range ($n_{cis} = $ 5%–15%), the dimension of the polymer parallel to the oriented direction rather increases [Fig. 9(c)]. Then, after the breakdown of the smectic layers, a uniaxial shrinkage occurs under the N-I transition. Namely, the decrease in the translational order increases the shape anisotropy, while the uniaxial shrinkage is dominantly generated by the removal of orientational symmetry. The unique photomechanical deformation of Sm-A PRPs has already been reported [8,35].

A relationship among s, τ, and r is established to link the LC state with the accompanying conformational change in the polymer network during photoisomerization. It has been known that the shape parameter of the elastomer has a linear relationship with the orientational order parameter of the mesogenic units ($r = 1 + \alpha s$). In the previous study, we revealed that the uniaxial elongation during the Sm-A–N phase transition is attributed to the dispersed backbone chains. The shape parameter change in response to the variation in τ can be described using an exponential term [21]. Therefore, the final expression of r is given as follows:

$$r(n_{cis}) = 1 + \alpha s(n_{cis}) - [\exp\{\eta\tau(n_{cis})\} - 1]. \quad (42)$$

When $\tau = 0$, the smectic order is removed and the equation becomes identical to the original linear relationship. The macromolecular shape and LC structural parameters are utilized to derive the relationships in Eq. (42) for each PRP model. The resulting fitted curves (dotted lines) in Fig. 9 show good agreement with the data points (filled squares) obtained using the CG MD simulation. Table III lists the fitted coefficients, α and η, of the CLCP models. It shows that α increases with the spacer length. This result implies that a longer flexible chain not only improves the initial molecular alignment but also enables a larger photomechanical contraction under the same variation of s. The heavily crosslinked network structure also enhances the responsiveness of the PRPs. As the molar concentration of the crosslinker increases from 10 mol % to 40 mol %, α increases by about 11.4%–12.4%. In contrast to the tendency of variation in α, η decreases with increasing crosslinking ratio, which means that less elongation occurs during the collapse of the translational order. Zhang *et al.* [8] also reported that the densely crosslinked smectic polymer does not exhibit a distinct stretching behavior along the layer normal direction.

The photosoftening effect on the mechanical behavior of the PRP is also investigated. Figure 10(a) shows the generic stress-strain curves of the LCPs containing different amounts
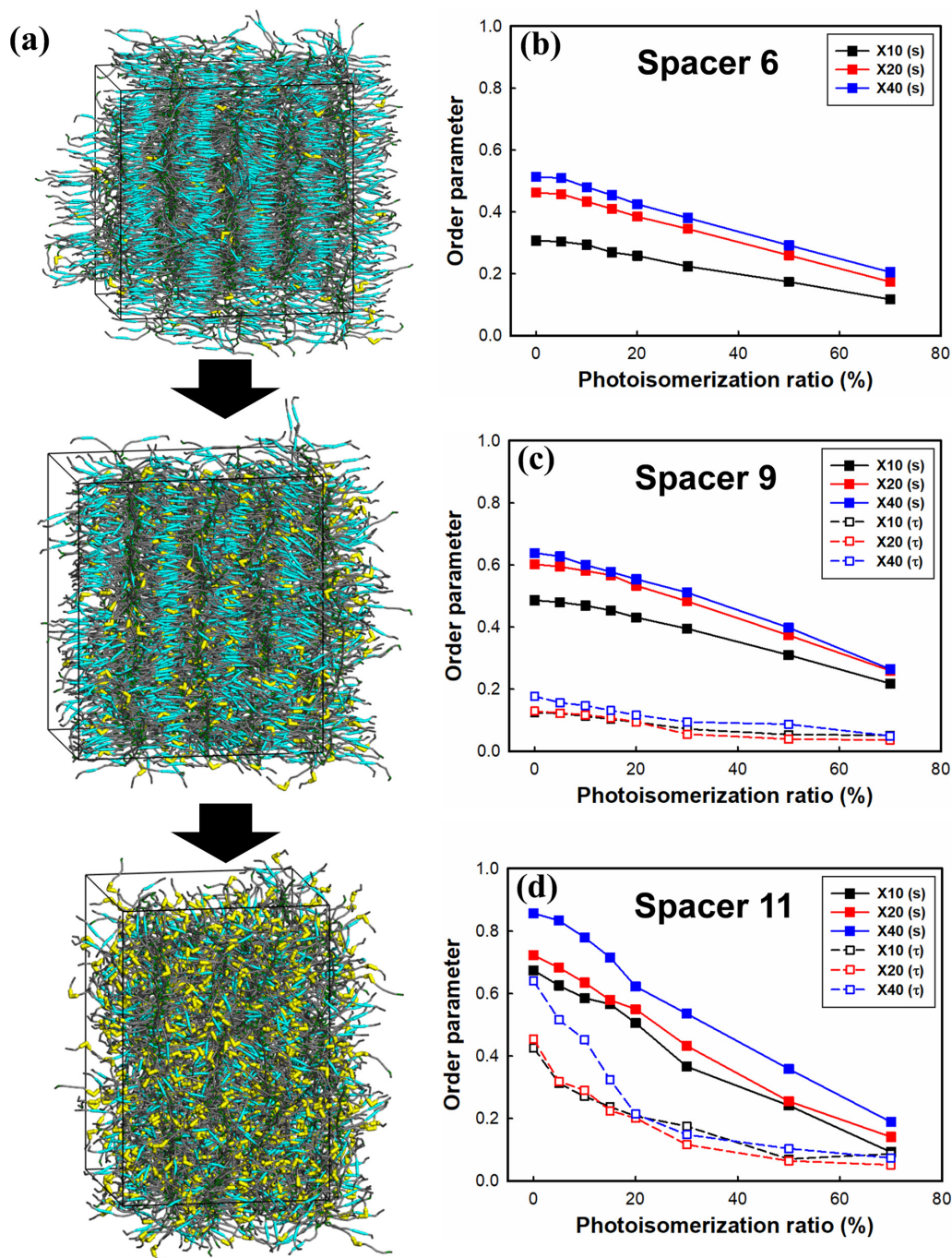
FIG. 8. (a) Light-induced phase transition of the CG MD model and the associated changes in the order parameters of (b) S6, (c) S9, and (d) S11 polymers.

of the isomerized molecules. The elastic modulus of the presented CG models ranges about 100–500 MPa, which is within the similar order of the reported mechanical properties of the glassy azo-LCP [46,47]. As n_{cis} increases up to 70%, the elastic modulus of the polymer network remarkably decreases by up to 55%. Another interesting feature is that the modification of the polymer structure and the corresponding changes in the LC phase can remarkably affect the mechanical responses. The nematic polymers with six methylene spacer units only have the shear modulus component, which reduces as the photochemical reaction proceeds [Fig. 10(b)]. As expected,

a more densely crosslinked LCP exhibits a larger value of μ. According to the classical rubber elasticity, μ is proportional to n_s, which is the average number density of polymer strands between two successive crosslinks. The smectic S9 and S11 CLCPs exhibit a much larger modulus for the layer dilation than the shear modulus of the elastomeric network itself, as shown in Figs. 10(c) and 10(d). In terms of molecular geometry, because the mesogen rods packed in the layer are closely located parallel to each other, the maximized $\pi-\pi$ stacking interaction yields the large mechanical resistance. The light-induced decrease in B is more impressive compared to that
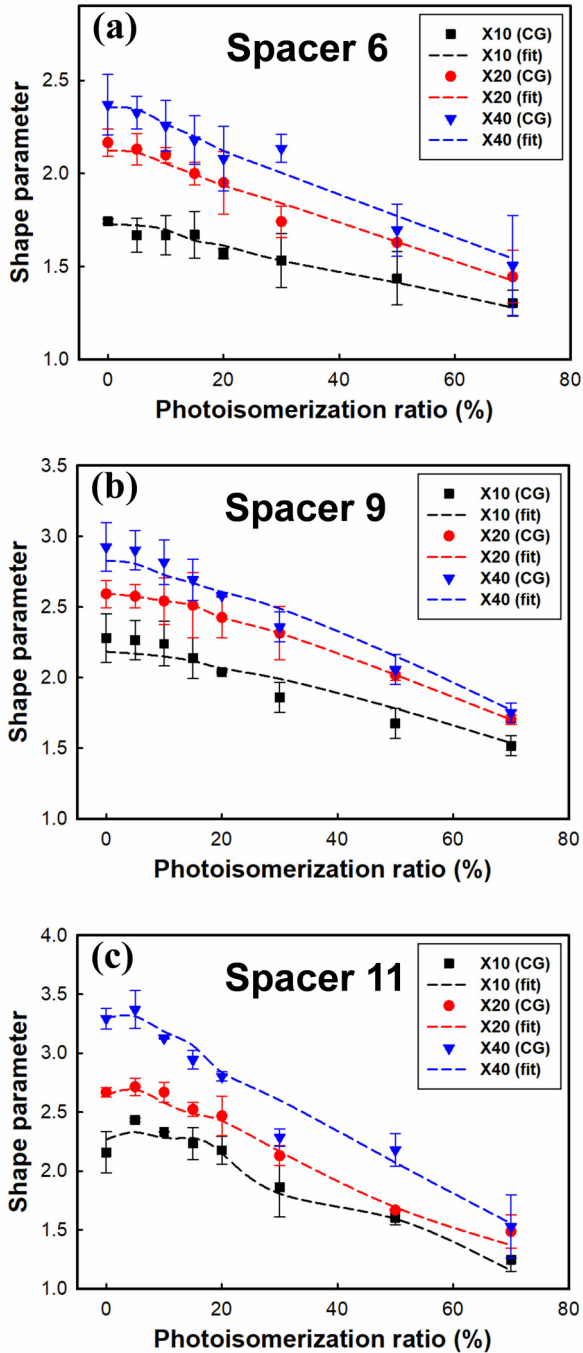
FIG. 9. Shape parameters of the PRP network models as a function of the photoisomerization ratio of the azobenzene molecules.

in μ. Indeed, the ratio of layer modulus to shear modulus (B/μ) reduces from 10 to 3 under the Sm-A–N transition. B still remains even after the phase transition is completed. If we allow B to drop to zero at a specific point, the computed μ rather increases under the molecular disordering, which is not desirable. The nonvanishing value of B is attributed to the curing and photoisomerization reactions at low temperature (300 K). Because the monomers are polymerized in the deep Sm-A phase, the crosslinked network memorizes its original structure at formation even under the photomechanical deformation. In addition, sufficient molecular mobility

to completely eliminate the positional order is not achieved due to the low external thermal energy. Figures 10(c) and 10(d) also show the dependence of the mechanical properties of smectic solids on the whole network morphology. As the number of spacer methylene units is changed from 9 to 11, B increases up to approximately 57%. Moreover, the improvement in the elastic moduli induced by increasing the crosslinking ratio is more pronounced for the S11 system. As shown in Fig. 8, a longer flexible spacer facilitates the enhancement of the LC symmetry of the polymer by modifying the degree of polymerization. That is, an increase in the crosslink density improves the mechanical properties of the PRP through a synergetic effect of rigidly connected polymer chains and a strong fixation of highly ordered LC units.

B. Photobending deformations

The CG-MD–FE coupling method is employed to simulate the macroscopic photobending behavior of the PRP film. Figure 11 shows the one-side clamped FE model, where $L_x = 20$ mm and $L_y = 2$ mm are the length and width of the PRP specimen, respectively. The length-to-thickness ratio ($L/h = 40$) is large enough for applying the plane stress assumption. The penetration depth-to-thickness ratio (d/h) is set to 0.4, and it is revealed that the gap between the linear and nonlinear solutions is distinct under this condition. The midplane of the strip is discretized by 20×4 rectangular lattices, and each lattice contains four overlaid triangular shell elements. As seen in Fig. 11, the uniform nematic directors $[n_0 = (1, 0, 0)^T]$ are individually defined at each element. The unpolarized UV ray is irradiated from the top of the PRP film along the z direction.

Figure 12 shows the evolutions of the bending curvature of the PRP films, which are composed of different macromolecular structures. The deflection curve in the xz plane is fitted by the third-order polynomial function, and the curvature of the bent strip is computed at the clamped point of the midplane. As seen in Fig. 12(a), in general, the nematic films bend toward the light source due to the spatial gradient of the light-induced contractile strain. The nonlinear bending behavior becomes profound when light penetrates deeply into the polymer domain. If I_{eff} reaches a specific point, the curvature rather starts to decrease because the in-plane shrinkage becomes more dominant. Figure 12 also shows two notable effects of the highly polymerized LCP structure on the macrodeformations: (i) increase in the maximum bending curvature and (ii) delayed bending speed to achieve the maximum point. These observed phenomena were also reported by Yu *et al.* [45]. As stated in Sec. III A, the linking between the polymer backbones makes the LC moieties more aligned to the uniaxial director, which enables a larger polymeric shape change during the photoreaction. Figures 13(a), 13(b), and 13(c) show variation in the spatial gradient of the ratio between the current and initial shape parameters (r/r_0) in response to the gradual photoisomerization reaction. Under the same external light condition, the r of a more compactly crosslinked PRP is more drastically changed. This result is consistent with the mesostructural changes observed using the CG MD analysis. As listed in Table III, the mesogenic order-shape coupling parameter (α) increases with the increment of crosslink density, which means that the LCP responds
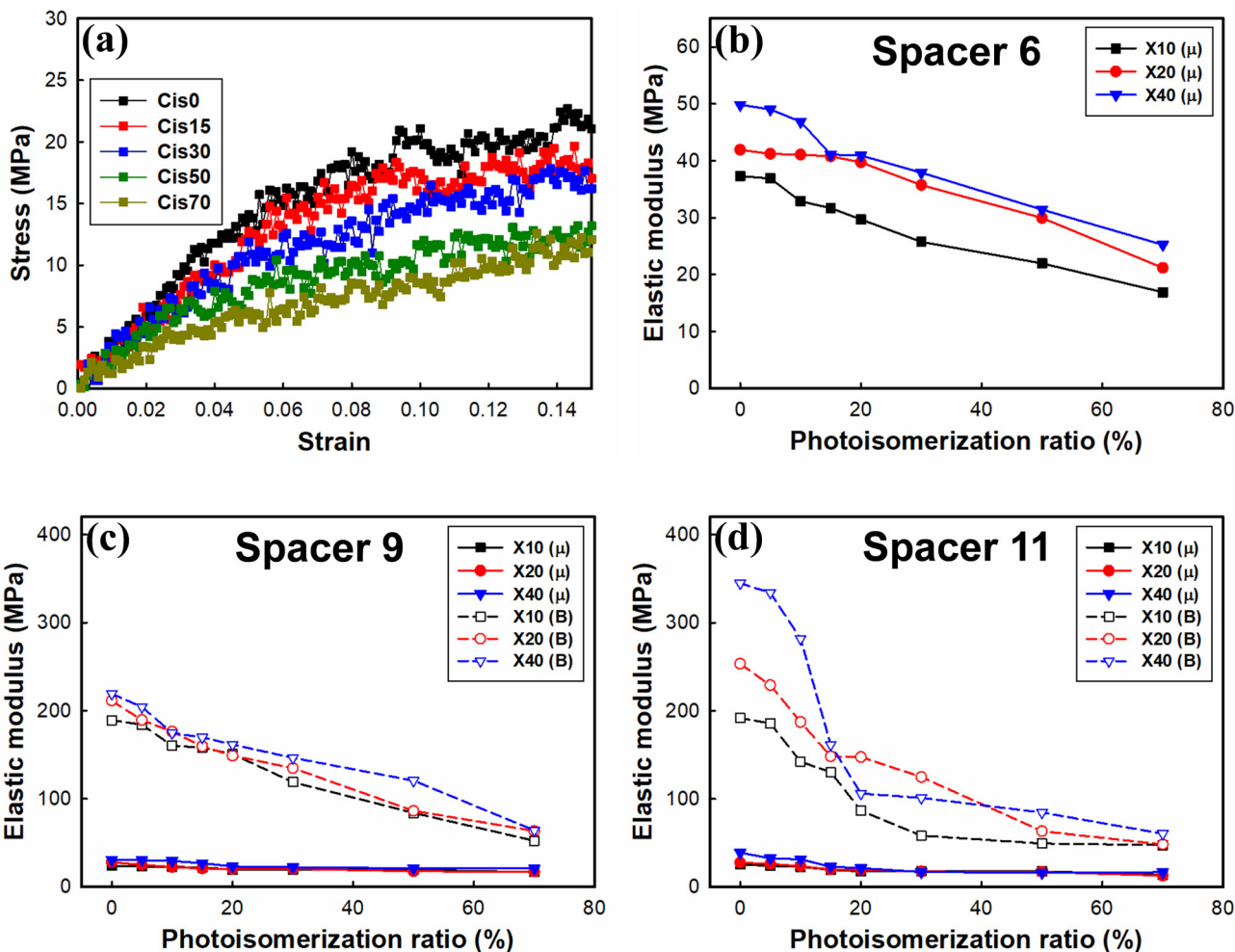
FIG. 10. Light-induced changes in (a) the stress-strain curves and (b)–(d) the elastic moduli of the PRPs.

more sensitively to the light-induced molecular disordering. A wide variation range of r for a highly crosslinked material, as shown in Fig. 9, contributes to a larger macroscopic photo-bending curvature. Meanwhile, the bending speed to achieve the maximum curvature is determined by the saturation point of the deformation gradient. Figure 8 shows that the LC order parameters of the loosely crosslinked network vanishes with smaller *cis*-fraction, which is equivalent to the lower light
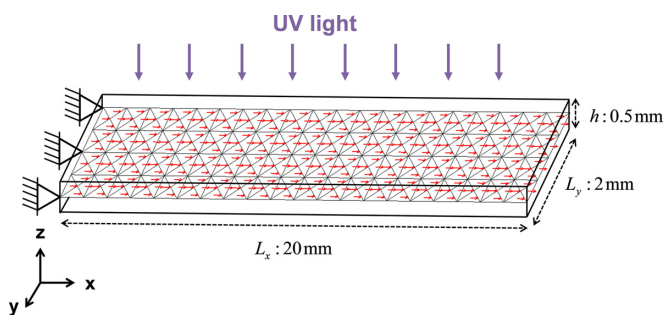
FIG. 11. Initial configuration of the flat FE model to describe the bending deformation of the PRP in response to the UV light illumination.

intensity. After the PRP becomes isotropic, no more remarkable photodeformation occurs. As shown in Fig. 13(a), the deformation gradient of the S11X10 system rapidly converges at $I_{eff} = 1.0$, where the curvature does not increase anymore. On the other hand, the variation in the shape parameter of S11X40 is still considerable at $I_{eff} = 2.0$ [Fig. 13(c)] and hence, it requires more light absorption to reach the maximum curvature.

The photoactivated deformation path is also dependent on the molecular length of the LC compounds. When we modify the spacer groups from S6 to S9, the overall curvature decreases regardless of the crosslinking density as shown in Figs. 12(a) and 12(b). The reduction in the photostrain is caused by the reinforced mechanical resistance with the aid of the compactly layered structure of the smectic S9 polymer. Figures 13(d), 13(e), and 13(f) show the elastic stiffness matrix component along the axial direction of the PRP film. A dominant stiffness degradation at the light-exposed surface demonstrates that the presented multiscale simulation scheme efficiently reflects the decaying light intensity with penetration depth and photosoftening effect on the mechanical properties of the LCP. Figures 13(d) and 13(e) clearly show that the modulus of the smectic S9 polymer is up to 80% larger than that of the S6 nematic
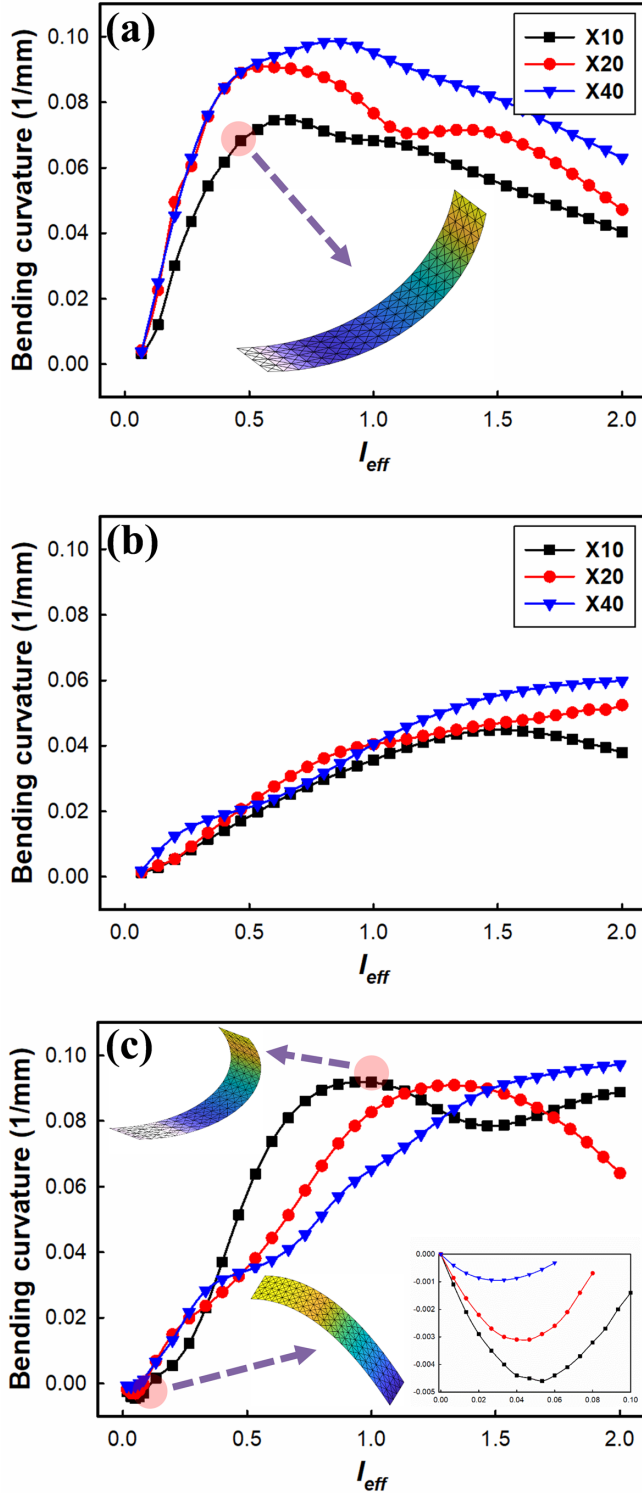
FIG. 12. Light-induced bending curvature of the FE LCP models with (a) 6, (b) 9, and (c) 11 methylene units in the spacer chains.

polymer. This enhanced mechanical property is attributed to the addition of the layer modulus (B), which is 3–10 times larger than μ of the elastomer, in constructing the internal stiffness matrix. Therefore, the photobending behavior of the LCP with nine methylene spacer units is more restricted.

On the other hand, under the same illumination level, the S11 polymers which have the largest layer modulus rather exhibit a larger curvature compared to S9 [Figs. 12(b) and 12(c)]. This is because the light-induced shape parameter change is large enough to overcome the effect of the enhanced modulus. Accordingly, we can indicate that the applicable range of the macroscopic photodeformation is determined by a trade-off effect between microscopic photostrain and the inherent mechanical resistance of the photoresponsive material.

Another notable feature is that the S11 polymers in the deep Sm-A phase show the switching of the photoactuated bending direction without moving the position of the light source. As shown in the inset of Fig. 12(c), a negative bending curvature is observed when I_{eff} ranges from 0 to 0.1. Under the weak light intensity, as commented in Sec. III A, the breakdown of the smectic layered structure rather leads to the elongation of the molecules along the oriented direction. Hence, the S11 PRP film initially bends opposite to the light source during the Sm-A–N transition due to the surface-dominant expansion mode. Next, as the light intensity is strong enough to cause the N-I transition, the bending direction is switched toward the luminous source due to the shrinkage behavior. However, as seen in Fig. 12(b), we cannot observe any distinct conversion of the bending motion for the spacer 9 system. This is because of the formation of an unstable smectic phase, which possesses a relatively small translational symmetry ($\tau = 0.2$). In this case, the tensile deformation is negligible compared to the disordering-induced contraction. We conclude this section by indicating that the maximum deformation, responsiveness, and deformation path of the PRP can be precisely adjusted by designing the synthesis condition and microscopic architecture of the polymer network.

C. Disclination-mediated 3D deformations

In addition to simple bending of the PRPs with a uniform director field, exotic 3D photomechanical deformations enabled by the imprinted LC defects are simulated. First, we identify the optical texture of the PRP films incorporated with spatial variation of the LC director. A thin circular plate with a radius of 20 mm and a thickness of 0.5 mm is prepared. The domain is discretized into irregular shell elements by using Delaunay triangulation. A complex director profile is prescribed based on the disclination defects, which can be formed naturally in the Schlieren texture. The nematic disclination can be characterized as singularities of continuously varying director fields with defect strength m, which is relevant to the order of rotational symmetry around the central topological defect. The planar director components with this imprinted pattern can be expressed as

$$(n_x, n_y)^T = [\cos(m\theta + c), \sin(m\theta + c)]^T, \quad (43)$$

where $\theta = \tan^{-1}(y/x)$ and $c = \pi/2$ is an angle constant. Various optical topologies with $m = \pm 1, -1/2$, and $-5/2$ are generated. Next, a unique defect-mediated pattern, which is only observed in the smectic structure, is constructed. The disclination core in the smectic phase breaks the positional symmetry of the continuous lines of the self-assembled layers.
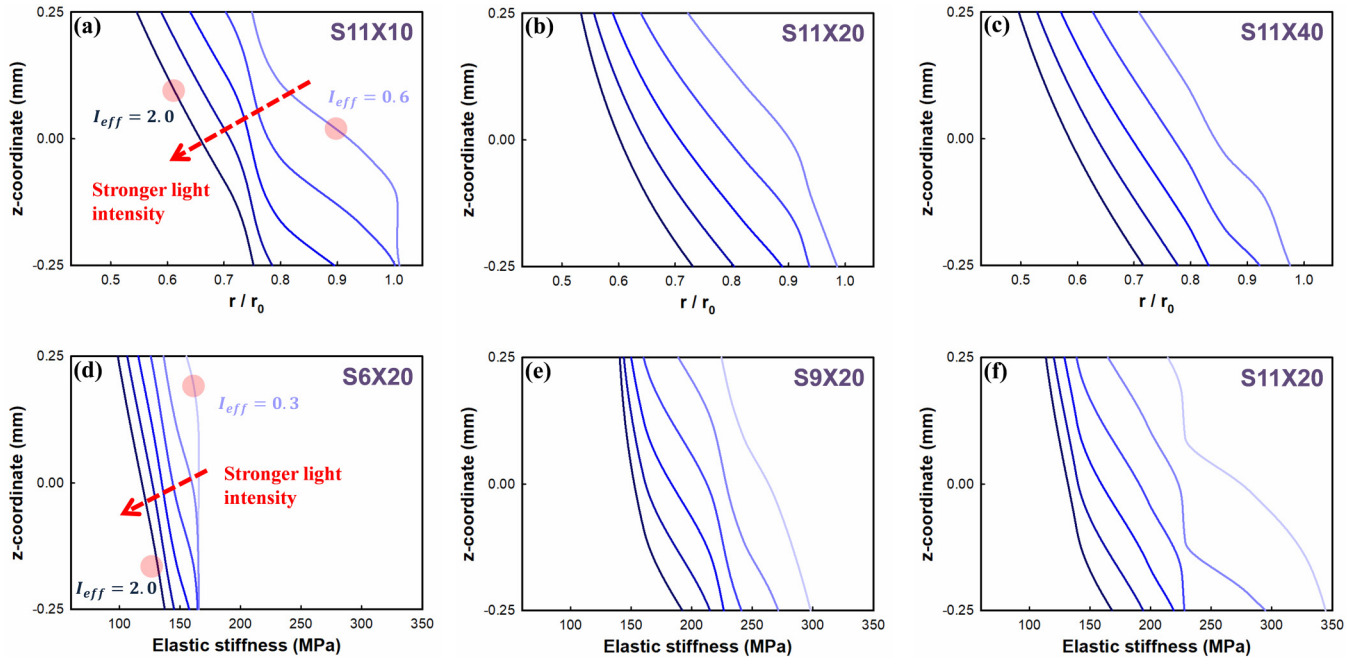
FIG. 13. Spatial profiles of (a)–(c) r/r_0 of the PRP films with different crosslinking ratios and (d)–(f) elastic stiffness component of the polymers with different spacer groups.

Here, the layer structures in the vicinity of $\pm 1/2$ disclination cores combined with elementary dislocations are modeled. Energetically stable configurations can be obtained by minimizing the distortion free energy of the smectics [48–50]. In treating the submicron-scale layered pattern of the smectic defects, the mesh size should be comparable to the layer spacing (about 3–4 nm). Therefore, a smaller sample with a radius of 60 nm and a thickness of 1.5 nm is additionally prepared. The interval between the allocated meshes is set to approximately 3 nm.

Figures 14 and 15 show the deformed configurations of the PRPs with a disclination-mediated nonuniform molecular alignment. Clamped and simply supported boundary conditions are applied to the edge of the circular specimen, and the resulting optical textures are subtly different. The nematic S6 LCP network imprinted with the $m = 1$ azimuthal defect deforms to the cone-shaped configuration under the light-induced phase transition from nematic to isotropic state. More complex morphologies can be manufactured by modifying the defect strength of the disclination topology. These simulated configurations with different prescribed patterns are fairly consistent with the complex surfaces obtained experimentally [7]. Note that, as seen in Figs. 14 and 15, the 2D plane of the smectic CLCP is sequentially transformed into two different configurations under light illumination. Initially at $I_{eff} = 0$–1, the polymers with 11 spacer units undergo the Sm-A–N transition and reach the first equilibrium state, whose configuration cannot be realized in the photoresponse of the nematic solids. Thereafter, as the light intensity increases sufficiently to convert the deformation modes, the patterned specimen jumps to another distinct state and its final topography is similar to that developed during the N-I transition. The results indicate that the PRP domain, which possesses both inherent characteris-

tics of the smectic solids and engineered inhomogeneity in the molecular director, can be utilized as a self-deformable structure with multiple programmed shapes.

Next, the light-induced macroscopic topographies of the LCPs incorporated with the smectic layer defects are examined. Figure 16 shows the smectic layer configuration, normal director distribution, and stepwise photodeformations of the S11 PRPs with $\pm 1/2$ disclination charges. The red dotted lines indicate the position where the magnitude of layer ordering is maximized. The LC directors are assigned perpendicular to the tangential lines of the 2D smectic layers. As shown in Fig. 16(a), a representative pattern with $m = 1/2$ has a single dislocation at the center and arc-shaped layers at the left half of the plane. This texture is generated to have a uniform spacing and make the curvature of the layers disappear under the mathematical minimization of the distortion free energy. Meanwhile, the microstate distribution with $m = -1/2$, as presented in Fig. 16(b), resembles that observed in the nematic topology with the same defect strength. These numerical examples prove that the engineering of the smectic order can also be an alternative way to realize the complex shapes that are different from those of the nematic polymers. Despite a lack of utilization of the disclinations in smectics as the photoresponsive surfaces, these novel structures can be converted into more exotic shapes compared to the PRPs imprinted with conventional patterns.

IV. CONCLUSIONS

In this work, a multiscale photomechanical simulation framework is proposed to efficiently integrate the mesoscopic and continuum-mechanics models. The CG MD technique is

LC director field	**N → I (S6)**	**Sm A → N (S11)**	**N → I (S11)**

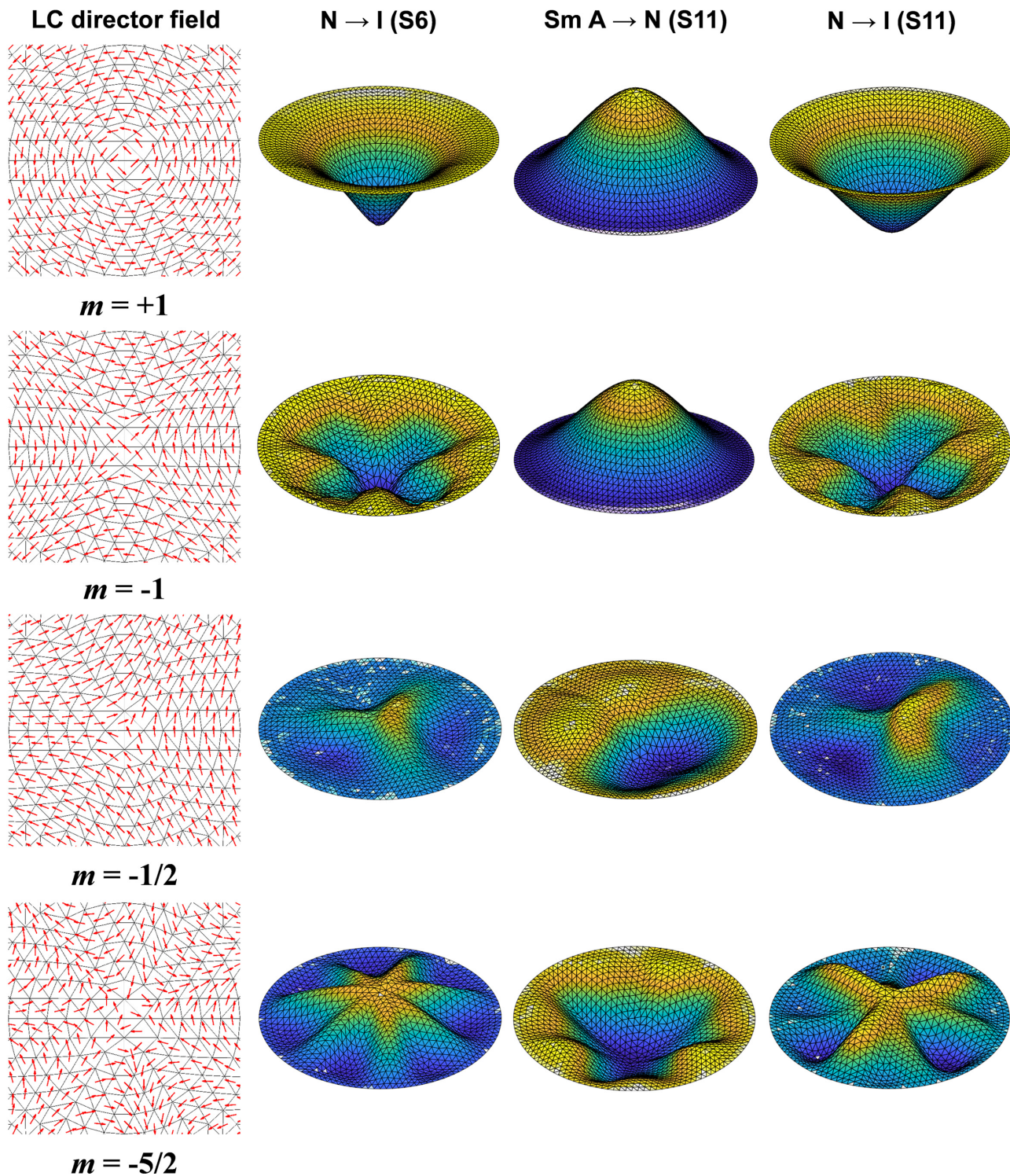
$m = +1$
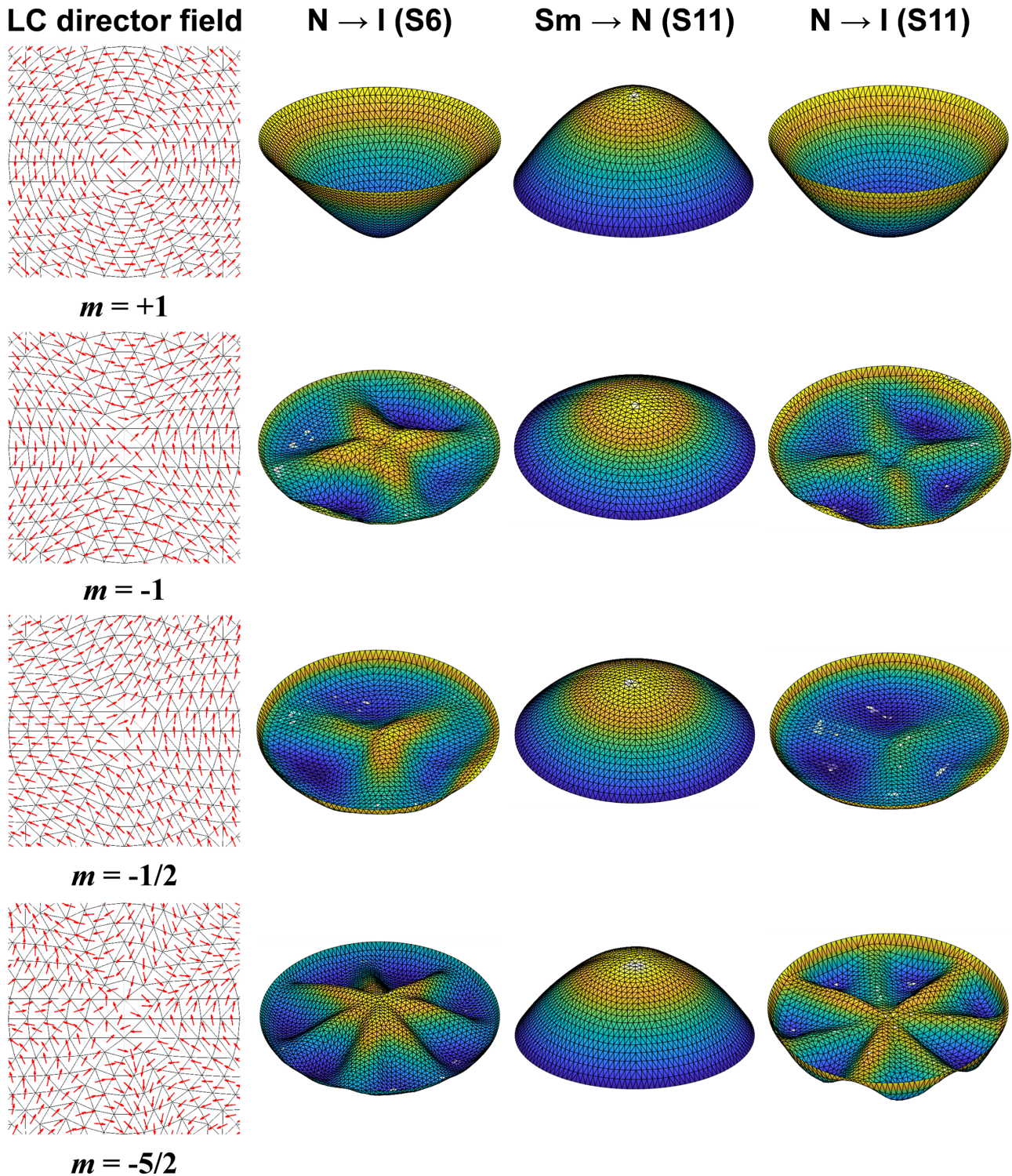
$m = -1$

$m = -1/2$

$m = -5/2$

FIG. 14. Optical textures of the photoresponsive surfaces with various polymeric structures and preprogrammed director distributions. Edge boundary condition: clamped.

utilized to reduce the DOFs and predict the global response of the macromolecules. The IBI-based CG interaction sets precisely reproduce the conformational characteristics and mesophase behavior of the azobenzene-containing LCP network. Specifically, the mesoscale photoswitching potentials are developed to reproduce variations in the microstructure under UV light illumination. Then, the mesoscale photoisomerization simulation is conducted to observe two distinct multiphysical phenomena: (i) polymeric shape change under the light-induced phase transition (Sm-*A*–N–I) and

FIG. 15. Optical textures of the photoresponsive surfaces with various polymeric structures and preprogrammed director distributions. Edge boundary condition: simply supported.

(ii) degraded mechanical property, which arises from molecular disordering. A relationship between the order parameters of the mesogenic units and the shape parameter of the entire polymer network is defined to quantify the molecular-scale photodeformations. In addition, the shear and smectic layer moduli of the PRPs with different photoisomerization ratios are computed from their stress-strain curves. The mesoscale mechanical parameters are inserted into the continuum FE model as a form of the inhomogeneous photostrain and elastic modulus profiles in terms of the external light intensity. Finally, a large-scale photomechanical behavior of PRP is realized using a 3D tensorial form of the light-
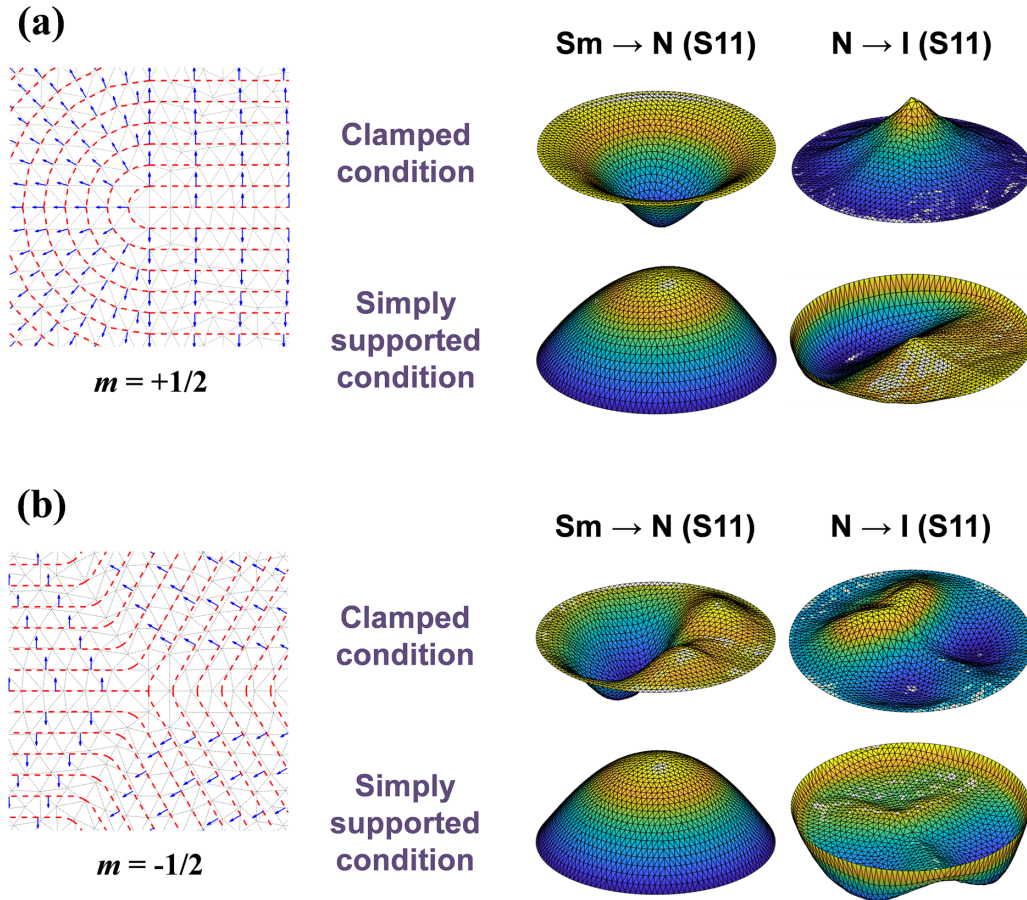
FIG. 16. Light-induced macroscopic deformations of the PRP specimens incorporated with smectic topological defects.

mechanical coupled constitutive relation, which is based on the neoclassical elasticity theory. Especially, the geometric nonlinearity, which stems from the large rigid-body rotation during the photobending deformation, is implemented into the FE simulation by exploiting the EICR method.

Integration of the CG MD analysis with the continuum model enables us to treat the mesoscopic design parameters of the LCP network, which cannot be captured using the conventional AA MD simulation. We reveal that the modulations of the complex LC phase, the spacer length, and crosslinking density influence the initial structure of the PRP and its corresponding photomechanical deformation path. In particular, while the decrease in the nematic order parameter reduces the conformational shape anisotropy, the collapse of the translational order generates an elongation behavior of the PRP network. The stress-strain response of the CG model shows a severe decrease of up to 55% in the elastic moduli under light illumination, which proves that the photosoftening effect on the local mechanical properties of the PRP is not negligible in examining continuum-scale deformations. Furthermore, an exotic 3D deformation with the aid of the blueprinted patterns as well as the simple photobending is achieved by employing the hybrid CG-MD–FE method. The photomechanical behavior of the one-side clamped films demonstrates that the applicable range of the photobending curvature and speed of the deformation are decided by the responsiveness of the

shape parameter and intrinsic mechanical resistance of the PRPs. This study also reveals that, unlike the behavior of nematic LCPs, the smectic solids with the disclinations of the positional symmetry can be sequentially deformed into two different configurations, which can be controlled by the external light condition.

The presented multiscale simulation provides a more reasonable solution compared to the previously developed continuum-scale analysis owing to the efficient descriptions of the mesoscale phenomena. Especially, a relation between the microscopic LCP morphology parameters and macroscopic photomechanical performance is systematically established for the first time. The results can be utilized to perform a simulation-based design and analysis to improve the light-to-mechanical energy conversion efficiency. Moreover, the nontrivial motions of PRPs, such as the switching of the bending direction and stepwise deformations into the multiple programmed shapes, can be realized using the presented numerical method. We, therefore, hope that the presented simulation framework contributes to the design of spatiotemporal photodeformations and development of advanced photoresponsive materials and soft robots.

[1] P. M. Hogan, A. R. Tajbakhsh, and E. M. Terentjev, Phys. Rev. E **65**, 041720 (2002).

[2] L. Hines, K. Petersen, G. Z. Lum, and M. Sitti, Adv. Mater. **29**, 1603483 (2017).

[3] S. Palagi, A. G. Mark, S. Y. Reigh, K. Melde, T. Qiu, H. Zeng, C. Parmeggiani, D. Martella, A. Sanchez-Castillo, N. Kapernaum, F. Giesselmann, D. S. Wiersma, E. Laug, and P. Fischer, Nat. Mater. **15**, 647 (2016).

[4] M. Yamada, M. Kondo, J. Mamiya, Y. Yu, M. Kinoshita, C. J. Barrett, and T. Ikeda, Angew. Chem. Int. Ed. **47**, 4986 (2008).

[5] J. Lv, Y. Liu, J. Wei, E. Chen, L. Qin, and Y. Yu, Nature (London), **537**, 179 (2016).

[6] B. A. Kowalski, T. C. Guin, A. D. Auguste, N. P. Godman, and T. J. White, ACS Macro Lett. **6**, 436 (2017).

[7] M. E. McConney, A. Martinez, V. P. Tondiglia, K. M. Lee, D. Langley, I. I. Smalyukh, and T. J. White, Adv. Mater. **25**, 5880 (2013).

[8] Y. Zhang, J. Xu, F. Cheng, R. Yin, C. C. Yen, and Y. Yu, J. Mater. Chem. **20**, 7123 (2010).

[9] J. J. Wie, M. R. Shankar, and T. J. White, Nat. Commun. **7**, 13260 (2016).

[10] L. T. de Haan, C. Sánchez-Somolinos, C. M. Bastiaansen, A. P. Schenning, and D. J. Broer, Angew. Chem. Int. Ed. **51**, 12469 (2012).

[11] S. K. Ahn, T. H. Ware, K. M. Lee, V. P. Tondiglia, and T. J. White, Adv. Funct. Mater. **26**, 5819 (2016).

[12] J. Garcia-Amorós, H. Finkelmann, and D. Velasco, J. Mater. Chem. **21**, 1094 (2011).

[13] Y. Wu, Y. Demachi, O. Tsutsumi, A. Kanzawa, T. Shiono, and T. Ikeda, Macromolecules **31**, 1104 (1998).

[14] A. Sánchez-Ferrer and H. Finkelmann, Soft Matter **9**, 4621 (2013).

[15] J. Choi, H. Chung, J.-H. Yun, and M. Cho, Appl. Phys. Lett. **105**, 221906 (2014).

[16] L. Golubović and T. C. Lubensky, Phys. Rev. Lett. **63**, 1082 (1989).

[17] L. Jin, Z. Zeng, and Y. Huo, J. Mech. Phys. Solids **58**, 1907 (2010).

[18] Y. Lin, L. Jin, and Y. Huo, Int. J. Solids Struct. **49**, 2668 (2012).

[19] H. Chung, J. Choi, J.-H. Yun, and M. Cho, Phys. Rev. E **91**, 042503 (2015).

[20] H. Chung, J. Choi, J.-H. Yun, and M. Cho, Sci. Rep. **6**, 20026 (2016).

[21] J. Moon, B. Kim, J. Choi, and M. Cho, Macromolecules **52**, 2033 (2019).

[22] C. Li, J. Moon, J.-H. Yun, H. Kim, and M. Cho, Polymer **129**, 252 (2017).

[23] H. Sun, J. Comput. Chem. **15**, 752 (1994).

[24] S. Plimpton, J. Comput. Phys. **117**, 1 (1995).

[25] M. Kondo, Y. Yu, and T. Ikeda, Angew. Chem. Int. Ed. **45**, 1378 (2006).

[26] T. Schneider and E. Stoll, Phys. Rev. B **17**, 1302 (1978).

[27] H. J. C. Berendsen, J. P. M. Postma, W. F. van Gunsteren, A. DiNola, and J. R. Haak, J. Chem. Phys. **81**, 3684 (1984).

[28] V. Varshney, S. S. Patnaik, A. K. Roy, and B. L. Farmer, Macromolecules **41**, 6837 (2008).

[29] I. Yarovsky and E. Evans, Polymer, **43**, 963 (2002).

[30] G. Milano, S. Goudeau, and F. Müller-Plathe, J. Polym. Sci. B: Polym. Phys. **43**, 871 (2005).

[31] D. Reith, M. Pütz, and F. Müller-Plathe, J. Comput. Chem. **24**, 1624 (2003).

[32] M. Warner and E. M. Terentjev, *Liquid Crystal Elastomers* (Clarendon, Oxford, 2003).

[33] A. K. Subramaniyan and C. Sun, Int. J. Solids Struct. **45**, 4340 (2008).

[34] J. M. Adams and M. Warner, Phys. Rev. E **71**, 021708 (2005).

[35] N. Aßfalg and H. Finkelmann, Macromol. Chem. Phys. **202**, 794 (2001).

[36] E. Nishikawa and H. Finkelmann, Macromol. Chem. Phys. **200**, 312 (1999).

[37] S. Conti, A. DeSimone, and G. Dolzmann, J. Mech. Phys. Solids **50**, 1431 (2002).

[38] Y. Yu, M. Nakano, and T. Ikeda, Nature (London) **425**, 145 (2003).

[39] H. Chung, J. Park, and M. Cho, Phys. Rev. E **94**, 042707 (2016).

[40] C. A. Felippa and B. Haugen, Comput. Methods Appl. Mech. Eng. **194**, 2285 (2005).

[41] K. Y. Sze, X. H. Liu, and S. H. Lo, Finite Elem. Anal. Des. **40**, 1551 (2004).

[42] C. A. Felippa, Comput. Methods Appl. Mech. Eng. **192**, 2125 (2003).

[43] J.-L. Batoz, K.-J. Bathe, and L.-W. Ho, Int. J. Numer. Mehods Eng. **15**, 1771 (1980).

[44] D. Corbett and M. Warner, Phys. Rev. E **77**, 051710 (2008).

[45] Y. Yu, M. Nakano, A. Shishido, T. Shiono, and T. Ikeda, Chem. Mater. **16**, 1637 (2004).

[46] A. Shimamura, A. Priimagi, J.-i. Mamiya, T. Ikeda, Y. Yu, C. J. Barrett, and A. Shishido, ACS Appl. Mater. Interfaces **3**, 4190 (2011).

[47] T. J. White and D. J. Broer, Nat. Mater. **14**, 1087 (2015).

[48] H. Aharoni, T. Machon, and R. D. Kamien, Phys. Rev. Lett. **118**, 257801 (2017).

[49] B. G. Chen, G. P. Alexander, and R. D. Kamien, Proc. Natl. Acad. Sci. USA **106**, 15577 (2009).

[50] Y. H. Kim, D. K. Yoon, H. S. Jeong, O. D. Lavrentovich, and H. T. Jung, Adv. Funct. Mater. **21**, 610 (2011).